Supplementary Information

Dual resistance ensures stable intermittent electrolysis of natural seawater

Lu et al.

Table of Contents

Supplementary Methods

Characterizations

X-ray diffraction (XRD) analysis was carried out via a Rigaku Smart Lab 9 kW diffractometer equipped with a Cu Kα radiation source (λ = 1.54056 Å). The diffraction patterns were recorded under standard operating conditions, and the obtained spectra were used to evaluate the crystallographic structure of the samples. Raman spectroscopy was performed on a HORIBA spectrometer. The samples were excited with a 532 nm laser at a constant power of 20 mW. X-ray absorption spectroscopy (XAS) at the Pt *K*–edge was measured at the 1W1B beamline of the Beijing Synchrotron Radiation Facility (BSRF). The data collected included both X-ray absorption near-edge structure (XANES) and extended X-ray absorption fine structure (EXAFS) data, which provided information on the electronic state and local coordination environment of the Pt species. High-resolution transmission electron microscopy (HRTEM) images were acquired using a Thermo Talos F200X G2 instrument operated under high-stability conditions. For scanning transmission electron microscopy (STEM) characterization, Thermo Scientific™ Talos F200X and Talos F200X G2 instruments were employed, both of which were operated at an accelerating voltage of 300 kV. Before microscopic observation, all the samples were carefully washed with ultrapure water to eliminate residual ions. X-ray photoelectron spectroscopy (XPS) measurements were conducted on a Thermo Fisher ESCALAB-250Xi spectrometer. All the spectra were calibrated against the C 1s peak at 284.8 eV, which served as a reference for binding energy correction.

Electrochemical measurements. The electrochemical measurements were taken with a CS1350Pro electrochemical workstation (Wuhan Corrtest Instruments Corp., Ltd.). A typical three-electrode system was employed in a homemade H-type electrolytic cell. A piece of Pt-oxo NPs or commercial Pt/C (Pt/C, Tanak, 20%), a carbon rod, and a Hg/HgO electrode with 1.0 M KOH as the inner reference electrolyte were used as the working electrode, counter electrode, and reference electrode, respectively. Natural seawater is the electrolyte. For the powder Pt/C samples, 2 mg of catalyst and 10 μL of 5% Nafion solution were dispersed in 1 mL of ethanol. The mixture was ultrasonicated for at least 30 min to form a homogeneous ink. All the ink solutions were carefully dropped on freshly treated carbon paper (CP) and allowed to dry naturally. The measured potentials were converted from Hg/HgO to a reversible hydrogen electrode (RHE) according to the following equation: E(RHE) = E(Hg/HgO) + 0.098 + 0.0592 pH − iR. All the potentials reported in this work were calibrated

against the RHE without additional description. The hydrogen evolution reaction (HER) polarization curves were recorded via linear sweep voltammetry (LSV) at a scan rate of 10 mV s^{-1} and were *iR* calibrated.

Flow-type seawater electrolysers

Nafion 115 (N115, DuPont) membranes were sequentially pretreated with 5 wt% H_2O_2, 1.0 M H_2SO_4, and deionized water at 80 °C for 1 h, cooled to room temperature, and washed with deionized water until the pH of the washing water reached neutral. Pt-oxo NPs or Pt/C was used as the cathode, and IrRu/Ti was used as the anode at 60 °C in natural seawater.

Computational details

All the DFT calculations and AIMD simulations were performed via the Vienna Ab initio Simulation Package (VASP)[1]. The projector augmented wave (PAW) pseudopotential[2] with the PBE generalized gradient approximation (GGA) exchange-correlation function[3] was utilized in the computations. The cut-off energy of the plane wave basis set was 500 eV, and a Monkhorst-Pack mesh of size 1 × 1 × 1 was used in K-sampling. In all the AIMD simulations, canonical ensemble (NVT) conditions were imposed by a Nose–Hoover thermostat with a targeted temperature of 300 K. The MD time step was 1 fs, and all the systems were run for 10 ps to reach equilibrium. In the DFT calculations, the long-range dispersion interaction was described via the DFT-D3 method. The electrolyte was incorporated implicitly with the Poisson–Boltzmann model implemented in VASPsol++[4]. The relative permittivity of the media was chosen to be $\epsilon_r = 78.4$, corresponding to that of water. All the atoms were fully relaxed with an energy convergence tolerance of 10^{-5} eV per atom, and the final force on each atom was < 0.05 eV $Å^{-1}$.

Data availability

The data that support the plots within this paper are available from the corresponding author upon reasonable request.

Supplementary data

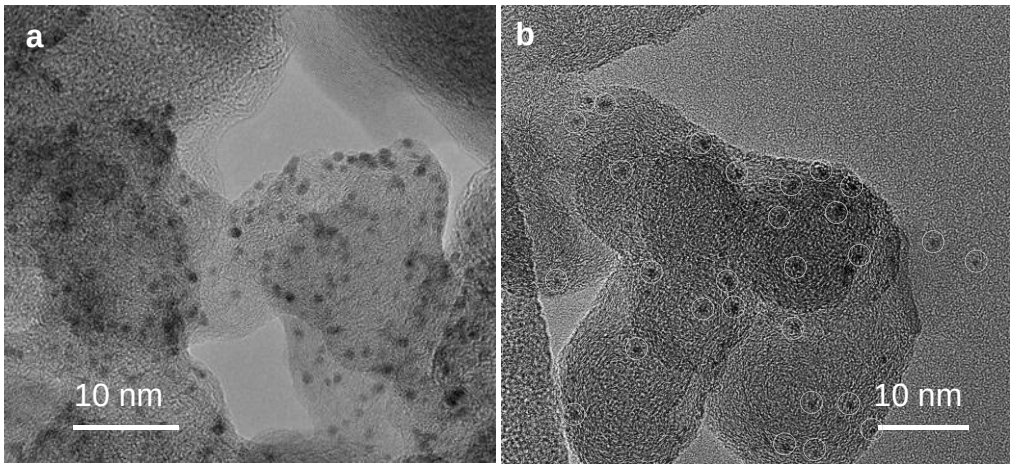

Supplementary Fig. 1 | Bright-field HRTEM images of Pt-oxo NPs.

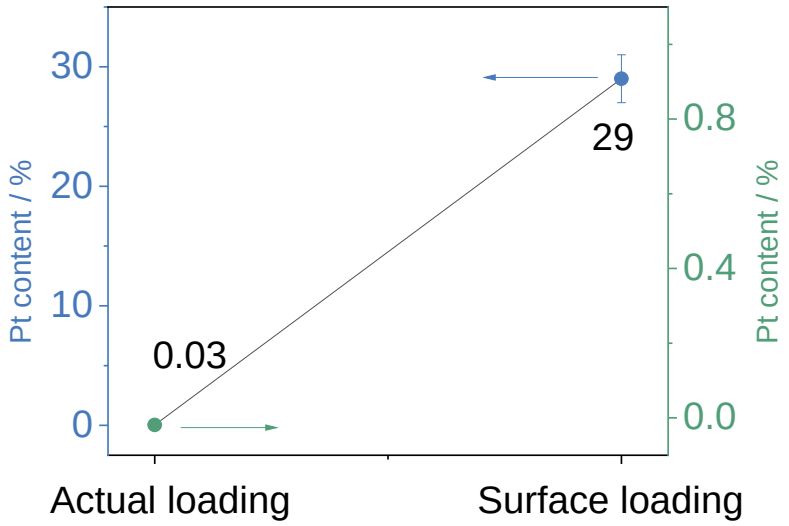

Supplementary Fig. 2| Surface and actual loading of Pt in Pt-oxo NPs.

Supplementary Note 1. The electrodeposition strategy effectively reduces the cost of Pt-based catalysts by significantly decreasing Pt consumption. Pt-oxo NPs were prepared via electrodeposition, with all Pt atoms deposited on the carbon support surface, greatly enhancing Pt atom utilization. This significantly reduces the Pt consumption and effectively lowers the cost of Pt-based catalysts.

The method for calculating the Pt surface loading is as follows:

First, the methylene blue (MB) molecule adsorption method was adopted to measure the surface area of the carbon supports.[5] Typically, the carbon support was added to a deionized water solution containing MB and kept at 25 ℃ for 48 hours to ensure that all accessible surfaces of the carbon support were covered by MB molecules. The changes in the concentration of MB were measured via UV–visible spectroscopy. The surface area of the carbon support was calculated from the concentration variation before and after adsorption via equation (1).

$$S_0=(C_0-C)V\times 2.45\times 10^6 \quad (1)$$

where S_0 is the surface area, C_0 is the concentration of the initial solution, C is the concentration of the adsorption equilibrium solution, V is the volume of solution added, and 2.45×10^6 m^2 is the area that 1 kg of MB can cover with the carbon material.

Then, we measured the surface area of 59 pieces of carbon support through the MB adsorption method and calculated the average surface area of one piece of carbon support to be 0.052 m^2 according to equation (1). Since the PtNa cluster can grow only on the outermost surface of the carbon support, calculating the mass fraction (wt%) of the PtNa cluster on the basis of the surface

mass of the carbon support is more accurate. The outermost surface of the carbon support was carefully scraped to obtain 1 mg of powder carbon support. With the same MB molecular adsorption method, the area of the carbon support powder was measured to be 0.34 m^2. Naturally, we established the relationship between the surface area (S_0) and surface mass (m_0) of the carbon support, which was 0.34 m^2 = 1 mg. Therefore, the surface mass of one piece of carbon support is (0.052 × 1)/0.34 =0.15 mg. Finally, the wt% of the metal-oxo nanoparticles was calculated via equation (2).

$$wt\%_{\text{PtNa cluster}} = \frac{m_{\text{Pt-oxo NPs}}}{m_{\text{Pt-oxo NPs}} + m_{\text{Carbon support}}} \quad (2)$$

where $wt\%_{\text{PtNa cluster}}$ was the mass fraction (wt%) of the Pt-oxo NPs, $m_{\text{Pt-oxo NPs}}$ was the mass fraction of the Pt-oxo NPs measured via ICP−MS, and the $m_{\text{Carbon support}}$ was 0.15 mg.

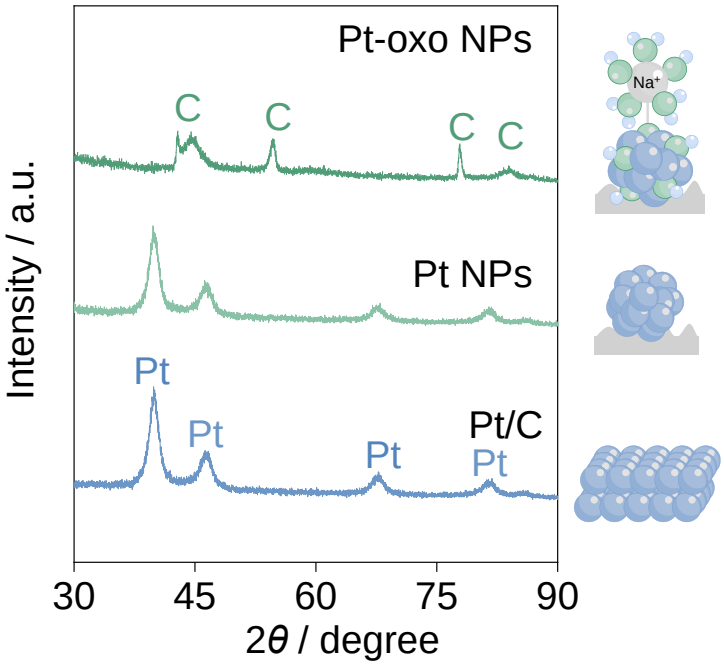

Supplementary Fig. 3 | XRD patterns of the Pt-oxo NPs, Pt NPs, and Pt/C.

Supplementary Note 2. As shown in the XRD patterns, the Pt-oxo NPs sample exhibits only carbon-related diffraction peaks (42.6°, 44.6°, 54.6°, 77.8°, and 83.8°, PDF #00-008-0415) without any detectable Pt signals, indicating that Pt exists in an amorphous state. In contrast, following H_2 reduction, the Pt NPs exhibit well-defined metallic Pt diffraction peaks at 39.9 °, 46.4 °, 67.5 °, and 81.4 ° (PDF #01-087-0640), resembling those of commercial Pt/C, confirming the formation of crystalline metallic Pt upon reduction.

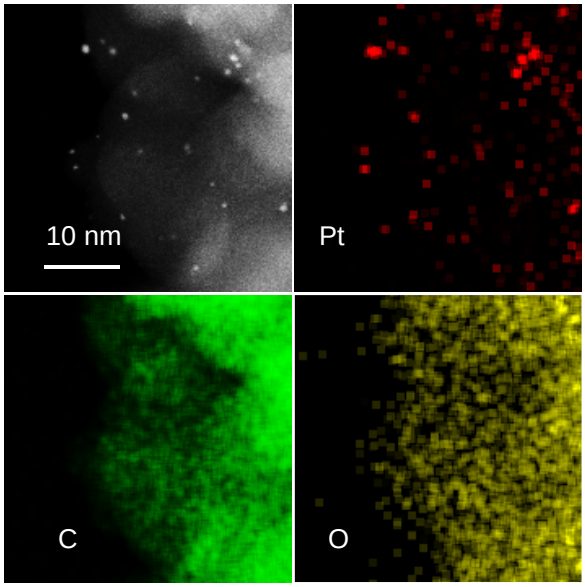

Supplementary Fig. 4| High-resolution HAADF-STEM image of Pt-oxo NPs. The corresponding element maps of the Pt-oxo NPs show distributions of Pt (red), C (green), and O (yellow).

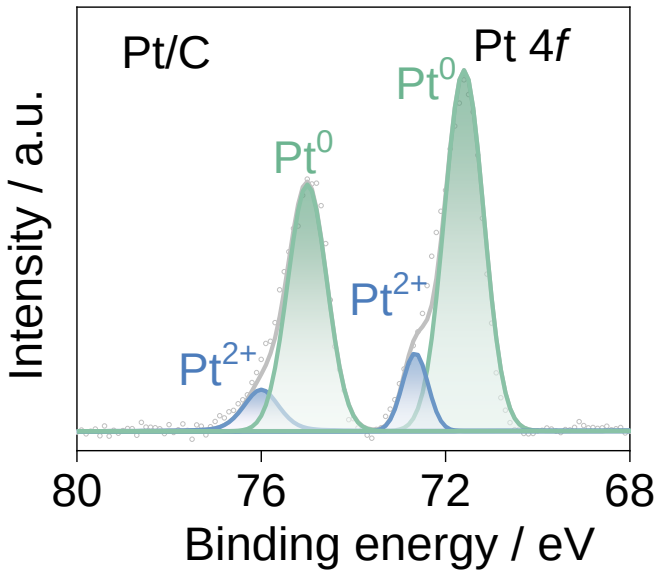

Supplementary Fig. 5| Pt 4f XPS spectra of commercial Pt/C.

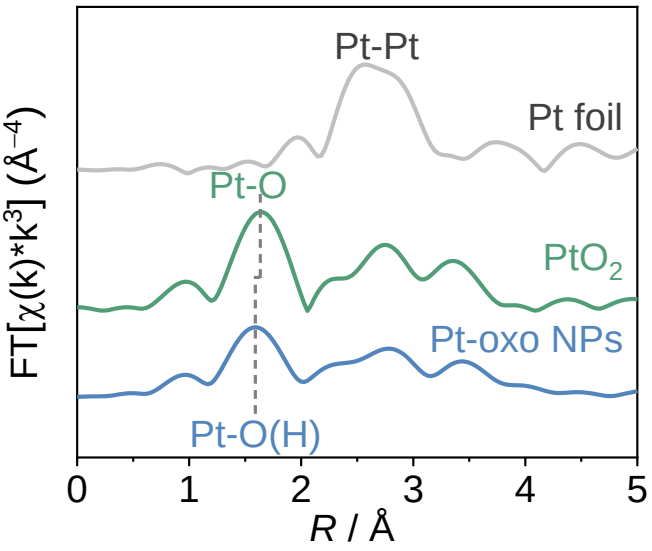

Supplementary Fig. 6| EXAFS spectra of the Pt-oxo NPs. PtO_2 and Pt foils are used as references.

Supplementary Table 1| Summary of recently reported HER in alkaline medium.

Catalysts	Electrolyte	Activity (mV) @ mA cm^{-2}	Ref.
Pt-oxo NPs	**Seawater**	**142@η10**	**This work**
Pt/VGAr-5	1.0 M KOH	124@η10	[6]
Ni nanoparticle	1.0 M NaOH	180@η10	[7]
Co-NRCNTs	1.0 M KOH	370@η10	[8]
CoP@BCN	1.0 M KOH	215@η10	[9]
CoS_2 NTA[a])/CC	1.0 M KOH	193@η10	[10]
Co_9S_8@NOSC[b)]	1.0 M KOH	193@η10	[11]
V-dopedNiS/NiS_2	1.0 M KOH	94@η10	[12]
Pt/G–CNFs	1.0 M KOH	177@η10	[13]
Pt/TC_2	1.0 M KOH	58@η10	[14]
p-WP_2	1.0 M KOH	175@η10	[15]
Fe/W-dopedNi_3S_2	1.0 M KOH	174@η10	[16]
Mo-NiCo-$LDH_{(Vo)}$	1.0 M KOH	194@η10	[17]

Supplementary Table 2| Summary of recently reported HER and OER performances for seawater electrolysis.

Catalysts	Electrolyte	Activity (mV) @ mA cm^{-2}	3-electrode Stability (h) @ mA cm^{-2}	Cell voltage	2-electrode Stability (h) @mA cm^{-2}	Ref.
HER						
Pt-oxo NPs	**Seawater**	**142@η10**	**4600@η1000**	**~2 V**	**3600@η1000**	**This work**
Mo_3Se_4-NiSe	Seawater	166@η10	50@η50	1.71 V	50@η10	[18]
R-CoC_2O_4@MXene	Seawater	160@η10	100@η10	—	—	[19]
Cr_2O_3-CoO_x	Seawater	220@η2	—	—	100@η500	[20]
Pt/MXene	Seawater	290@η10	250@η10	—	—	[21]
NiCoP/PC	Seawater	—	—	3.45 V	150@η500	[22]
NiCoP/PC	1.0 M KOH+ seawater	92@η100	1000@η1000	—	—	[22]
CoxMo2−xC/MXene/NC	Seawater	200@η10	225@η45	—	—	[23]
F-FeCoPv@IF	1.0 M KOH+ seawater	210@η1000	20@η100	—	100@η120	[24]
Cu_2S@NiS@Ni/NiMo	1 M KOH+ seawater	250@η1000	2000@η500	~2 V	2000@η500	[25]
Ru/MoO_2@$NiMoO_4$	1.0 M KOH+ seawater	184@η1000	50@η1000	—	—	[26]
Ru/$Cd_{0.02}Se_4$	1.0 M KOH+ seawater	6.3@η10	50@η10	—	—	[27]
Pt-Ni@NiMoN	1.0 M KOH+ seawater	11@η10	80@η200	—	—	[28]
Pt-Ni_3N@V_2O_3/NF	1.0 M KOH+ seawater	21@η10	100@η500	—	—	[29]
Ru-$Ni(OH)_2NW_2$/NF	1.0 M KOH+ seawater	130@η1000	70@η1000	—	—	[28]
Pt-Ni3S_2/Co_9S_8-Sv	1.0 M KOH+ seawater	18@η10	300@η100	2.1 V	50@η100	[29]
CN@NiCoS	1.0 M KOH+ seawater	8@η10	200@η1000	—	—	[29]
OER						
Cr_2O_3-CoO_x	Seawater	370@η32	220@η330		100@η500	[20]
MoO_3@CoO/CC	Seawater	370@η40	1000@η600		500@η1000	[30]
Mo-Ni_3S_2/NF	Seawater	370@η75	—	2.1 V	2500@η250	[31]
RuMoNi	1.0 M KOH+ seawater	245@η10	3000@η500	1.8 V	240@η500	[32]
CoFe-Ci @GQDs/NF	1.0 M KOH + 0.5 M NaCl	255@η100	2800@η1250	—	—	[33]

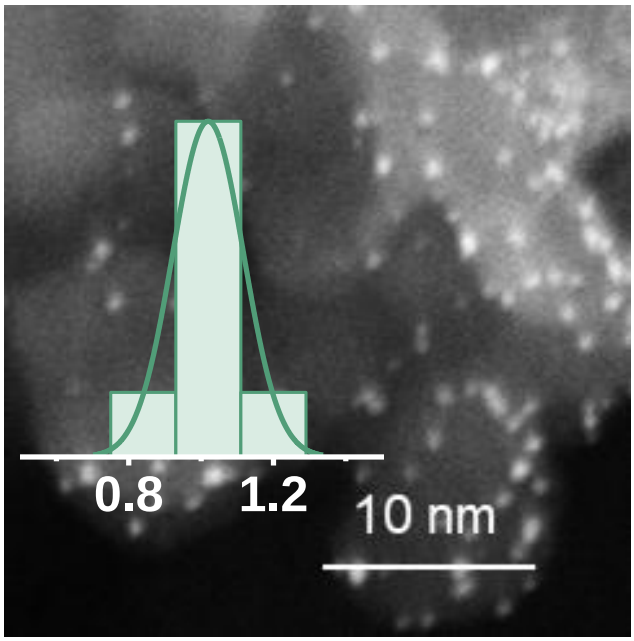

Supplementary Fig. 7| Structural characterizations of the Pt-oxo NPs after long-term intermittent durability test in natural seawater. HAADF-HRTEM image of the Pt-oxo NPs after long-term intermittent durability test in natural seawater. The insert is a distribution histogram of the particle size.

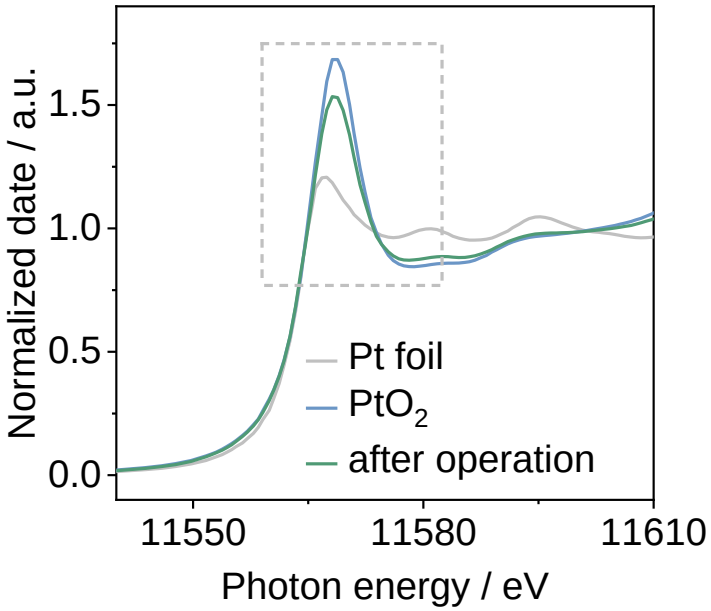

Supplementary Fig. 8| Structural characterizations of the Pt-oxo NPs after long-term intermittent durability test in natural seawater. XANES spectra of the Pt-oxo NPs after long-term intermittent durability test in natural seawater.

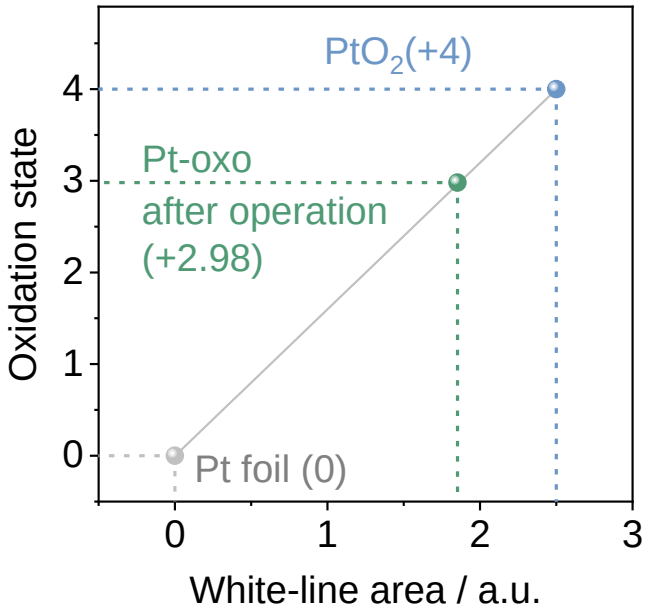

Supplementary Fig. 9| Structural characterizations of the Pt-oxo NPs after long-term intermittent durability test in natural seawater. Oxidation state of the Pt-oxo NPs after long-term intermittent durability test in natural seawater according to Supplementary Fig. 8.

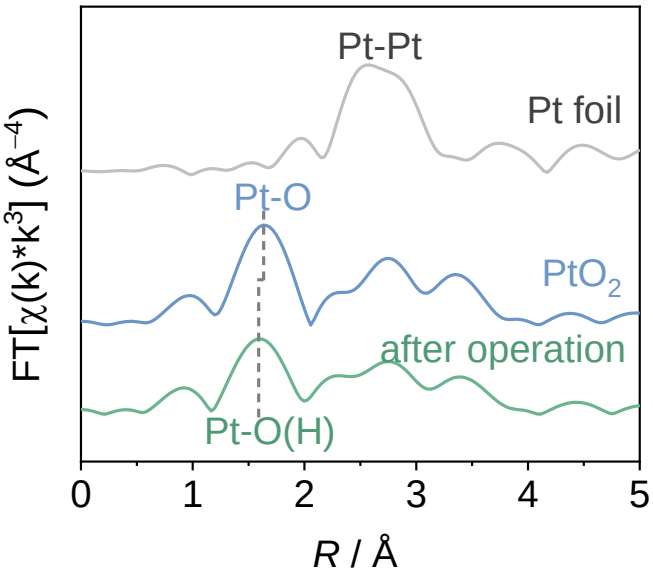

Supplementary Fig. 10| Structural characterizations of the Pt-oxo NPs after long-term intermittent durability test in natural seawater. EXAFS spectra of the Pt-oxo NPs after long-term intermittent durability test in natural seawater. The PtO_2 and Pt foil are used as references.

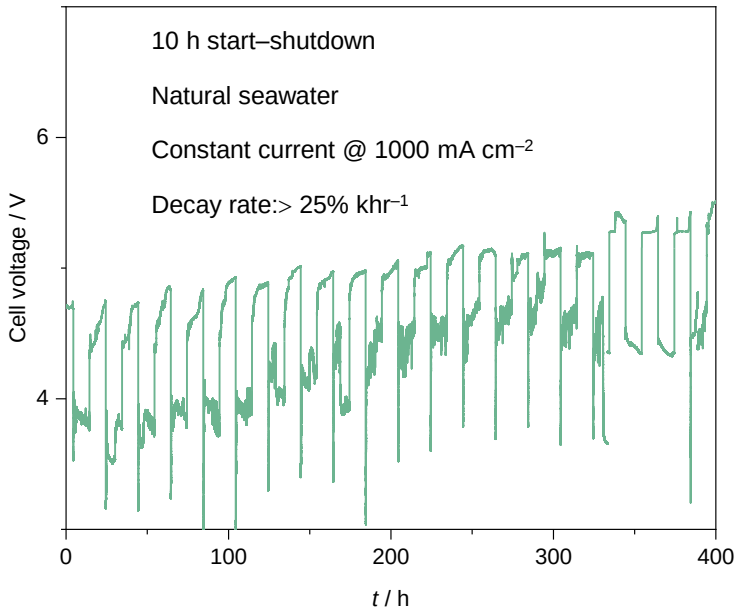

Supplementary Fig. 11| Intermittent durability test of Pt-oxo NPs at 1000 mA cm^{-2}.

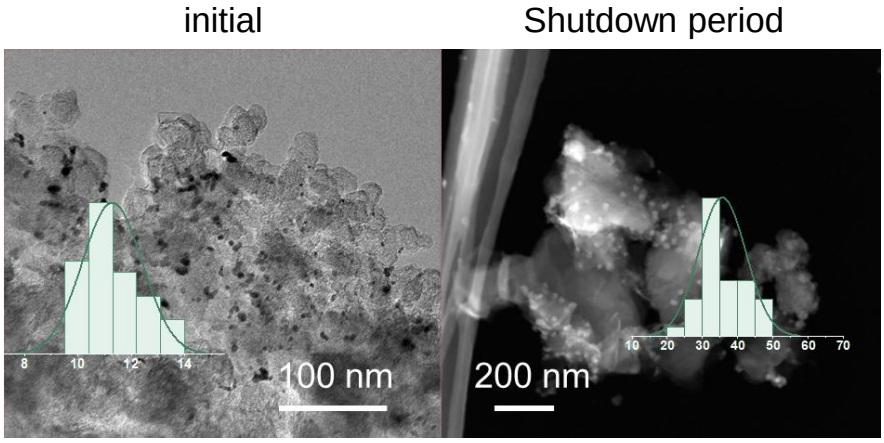

Supplementary Fig. 12| Structural characterizations of the Pt/C before and after long-term intermittent durability test in natural seawater. HAADF-HRTEM images of Pt/C (a) initially and (b) after long-term intermittent durability test in natural seawater. The insert is a distribution histogram of the particle size.

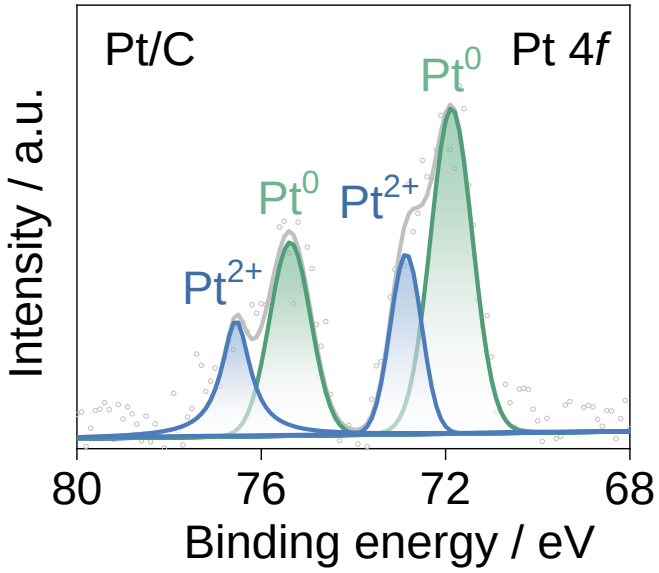

Supplementary Fig. 13| Structural characterizations of the Pt/C after long-term intermittent durability test in natural seawater. Pt 4*f* XPS spectra of Pt/C after long-term durability test.

Supplementary Note 3. Compared with the initial Pt/C (Supplementary Fig. 5), the proportion of Pt^{2+} in Pt/C after the intermittent durability test significantly increased (Supplementary Fig. 13), indicating that Pt was oxidized during the shutdown period.

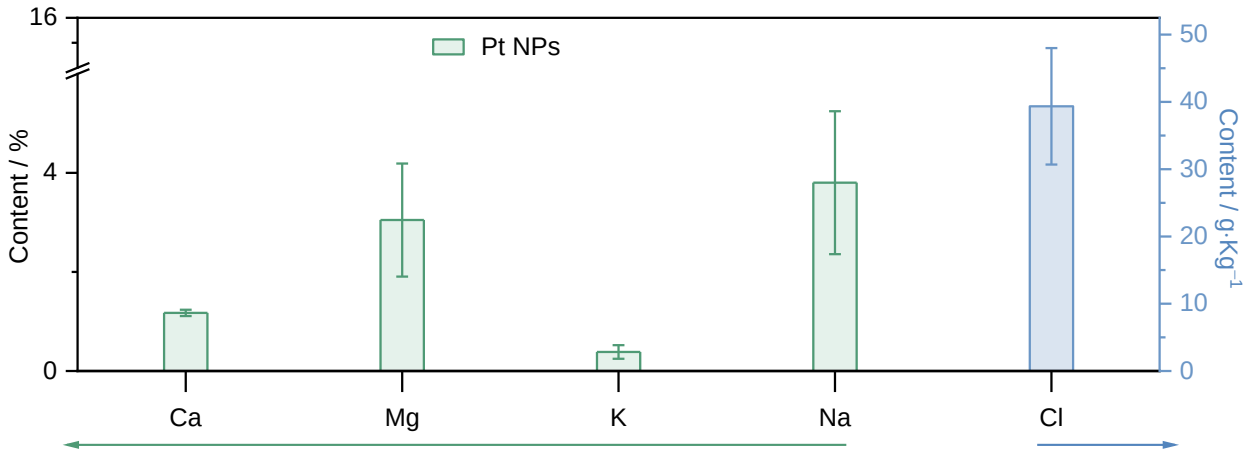

Supplementary Fig. 14| Residual amount of ions on the surfaces of the Pt NPs after HER, as measured via ICP–MS.

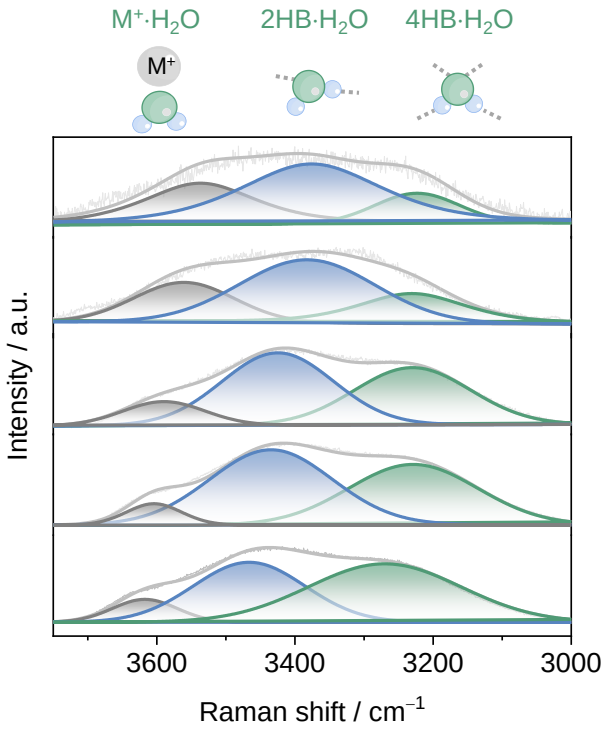

Supplementary Fig. 15| In situ Raman spectra of the Pt-oxo NPs recorded at –10 mA cm^{-2} in 1.0 M PBS.

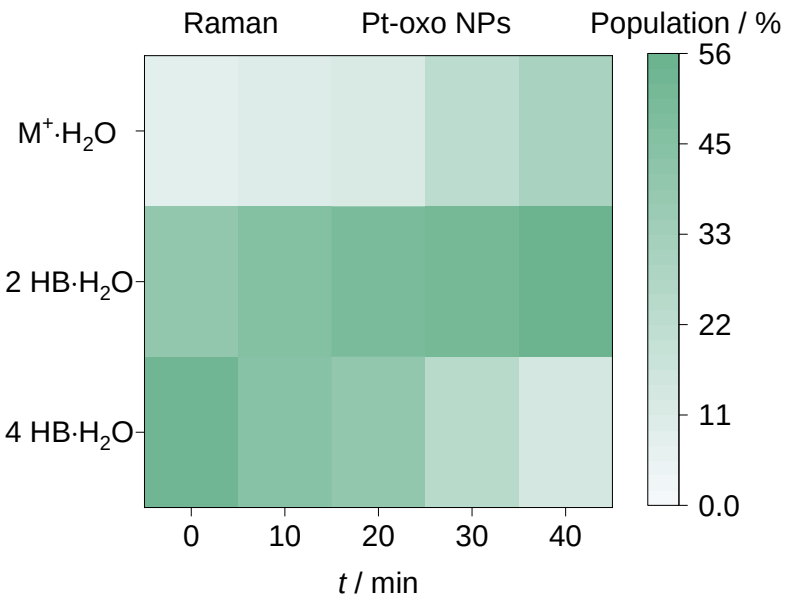

Supplementary Fig. 16| Calculated populations of the three O–H stretching modes from the time-dependent in situ Raman spectra at different reaction times from Supplementary Fig. 15.

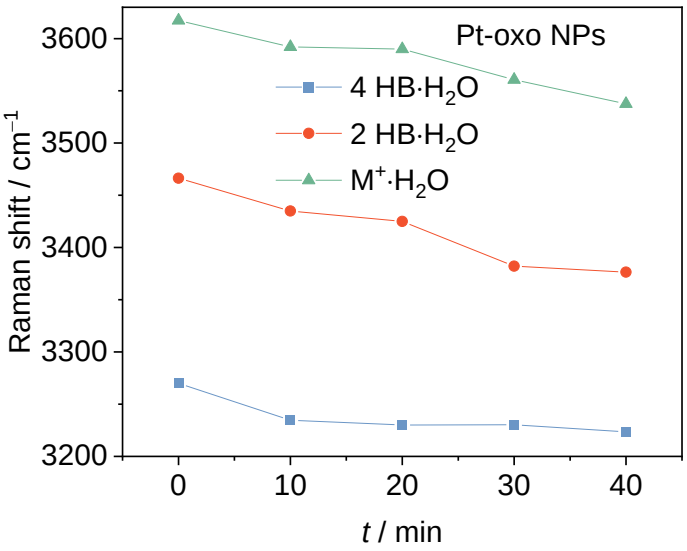

Supplementary Fig. 17| Time-dependent frequencies of 4-HB·H_2O, 2-HB·H_2O, and M^+·H_2O from Supplementary Fig. 15.

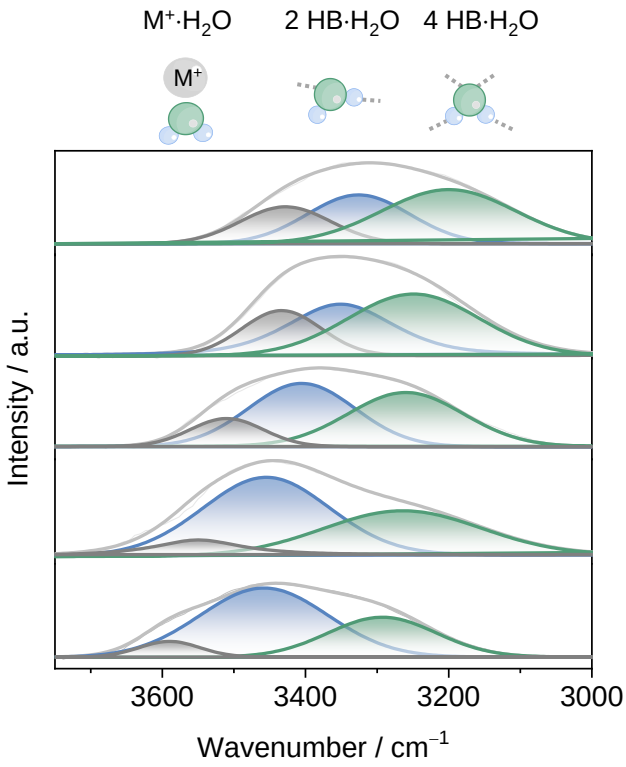

Supplementary Fig. 18| In situ ATR-FTIR spectra of the Pt-oxo NPs recorded at –10 mA cm^{-2} in 1.0 M PBS.

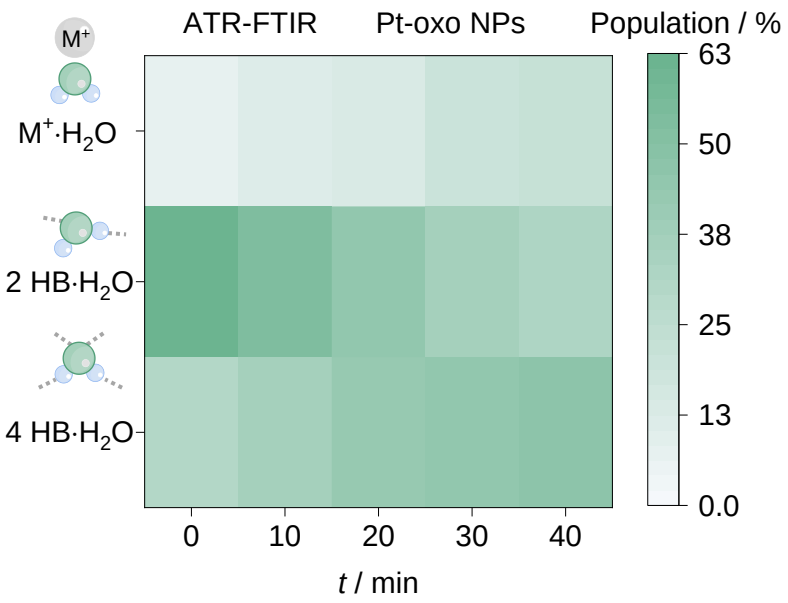

Supplementary Fig. 19| Calculated populations of the three O–H stretching modes from the time-dependent in situ ATR-FTIR spectra at different reaction times from Supplementary Fig. 18.

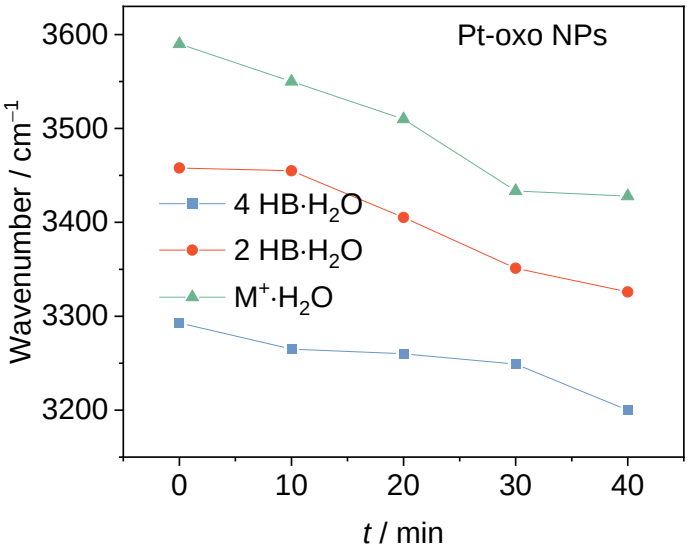

Supplementary Fig. 20| Time-dependent frequencies of 4-HB·H_2O, 2-HB·H_2O, and M^+·H_2O from Supplementary Fig. 18.

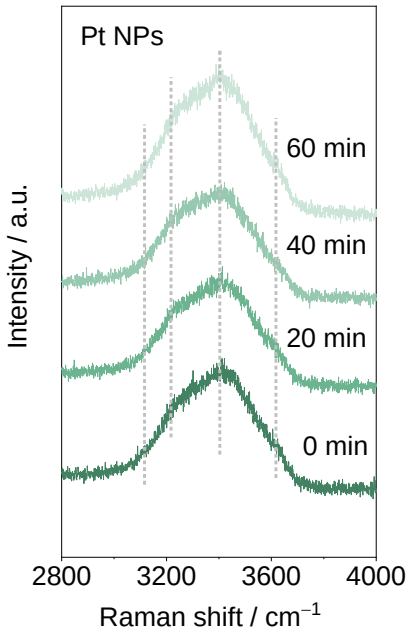

Supplementary Fig. 21| In situ Raman spectra of the Pt NPs recorded at –10 mA cm^{-2} in 1.0 M PBS.

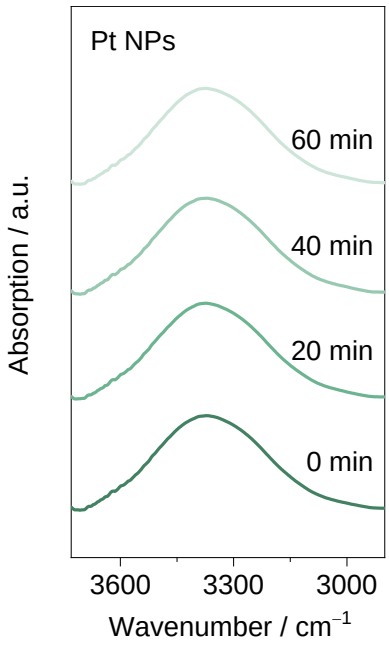

Supplementary Fig. 22| In situ ATR-FTIR spectra of the Pt NPs recorded at –10 mA cm^{-2} in 1.0 M PBS.

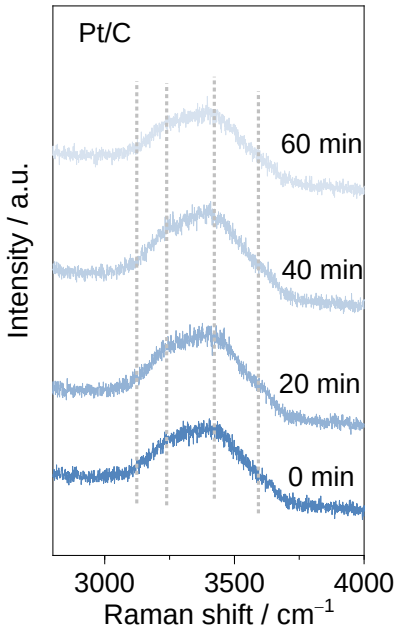

Supplementary Fig. 23| In situ Raman spectra of Pt/C recorded at –10 mA cm^{-2} in 1.0 M PBS.

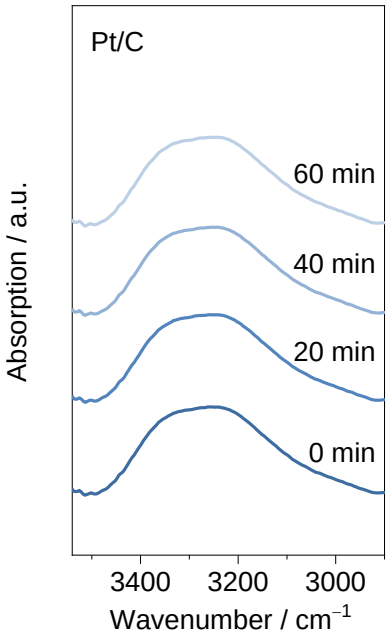

Supplementary Fig. 24| In situ ATR-FTIR spectra of Pt/C recorded at –10 mA cm^{-2} in 1.0 M PBS.

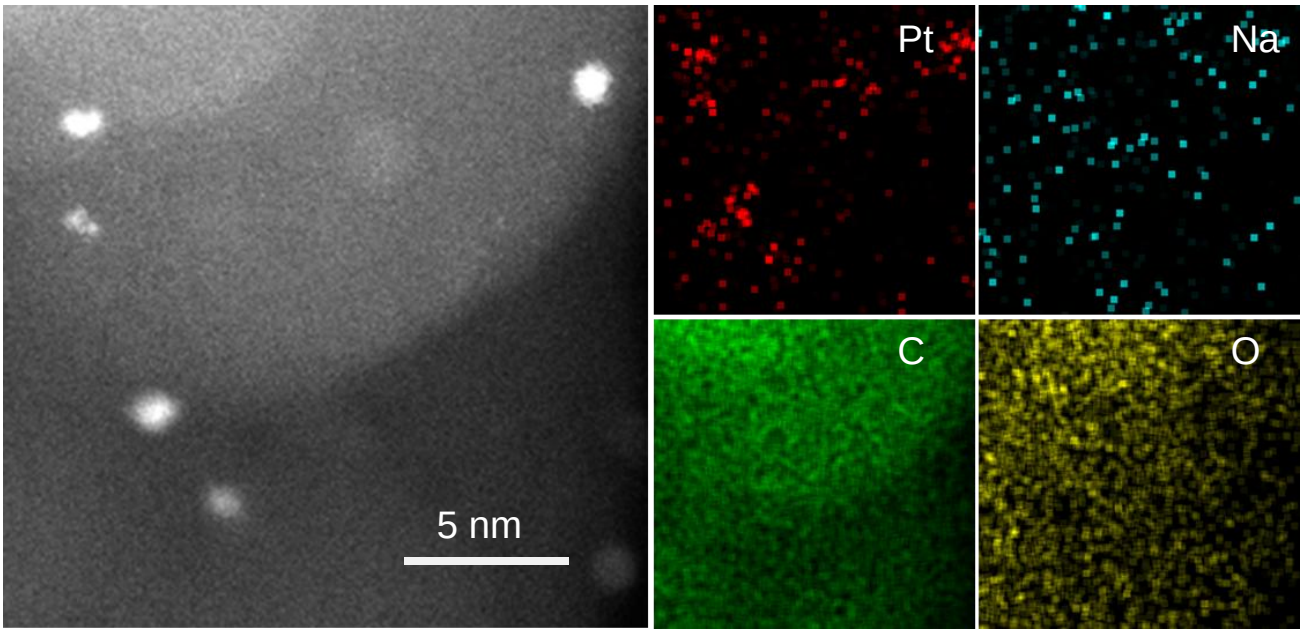

Supplementary Fig. 25| Elemental mapping images of the Pt-oxo NPs after intermittent DSE.

Supplementary Note 5. The Na is distributed on the surface of the Pt-oxo NPs after electrolysis (Supplementary Fig. 25).

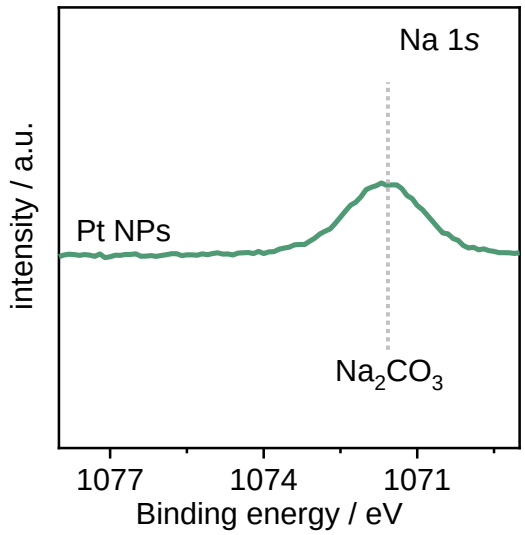

Supplementary Fig. 26| Na 1*s* XPS spectra of the Pt NPs after operation.

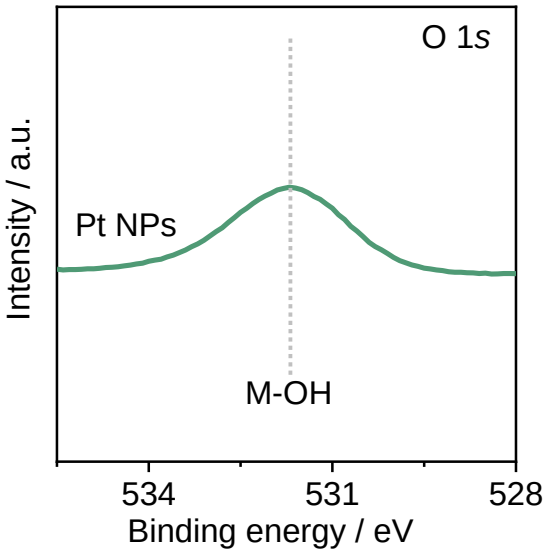

Supplementary Fig. 27| O 1*s* XPS spectra of the Pt NPs after operation.

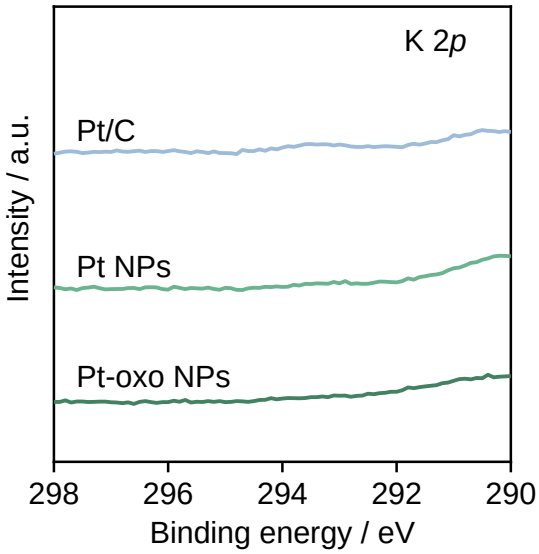

Supplementary Fig. 28| K 1*s* XPS spectra of the Pt-oxo NPs, Pt NPs, and Pt/C after operation.

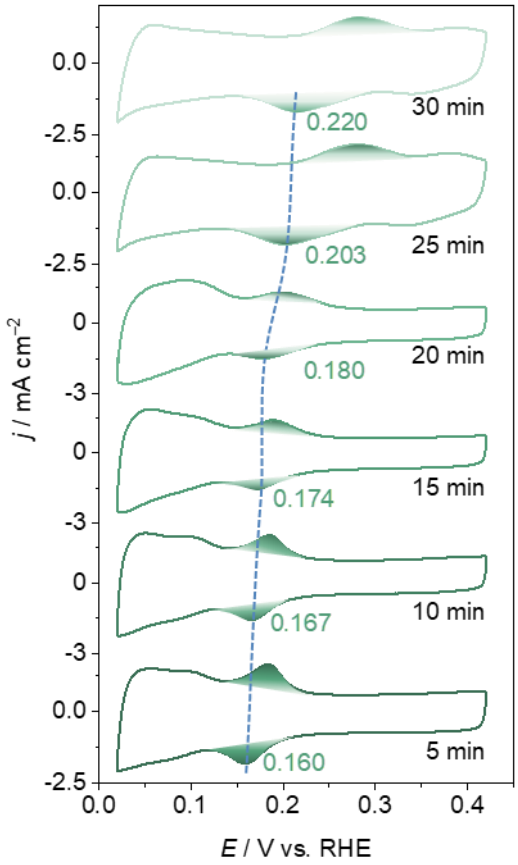

Supplementary Fig. 29| Cyclic voltammograms of the Pt-oxo NPs recorded in natural seawater.

Supplementary Note 5. During the electrodeposition process, a positive shift from 0.19 to 0.25 V vs. RHE in the characteristic vibrational peak of adsorbed OH^- on the surface of Pt is observed, indicating the accumulation of Na^+ on the Pt surface. This further suggests that Na^+ coordinates with the surface oxygen species of the Pt-oxo NPs, resulting in Pt-O-Na^+ linkages at the interface.

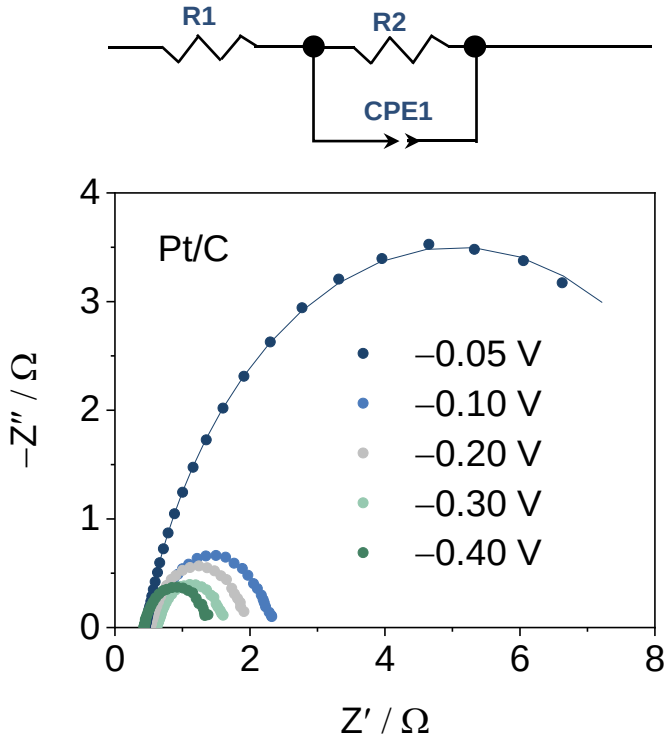

Supplementary Fig. 30| Potential-dependent EIS spectra of Pt/C at different applied potentials.

Supplementary Table 3. Potential-dependent Nyquist plots of Pt/C at different applied potentials.

η	Rs	T	P	Rct	Cdl
–0.05 V	0.44909	0.020973	0.82614	9.236	0.000424873
–0.10 V	0.62253	0.015938	0.84021	1.692	0.000451316
–0.20 V	0.53315	0.015474	0.85489	1.4139	0.000622164
–0.30 V	0.62587	0.01647	0.83639	1.0252	0.000411028
–0.40 V	0.43174	0.017874	0.85382	0.94684	0.000684

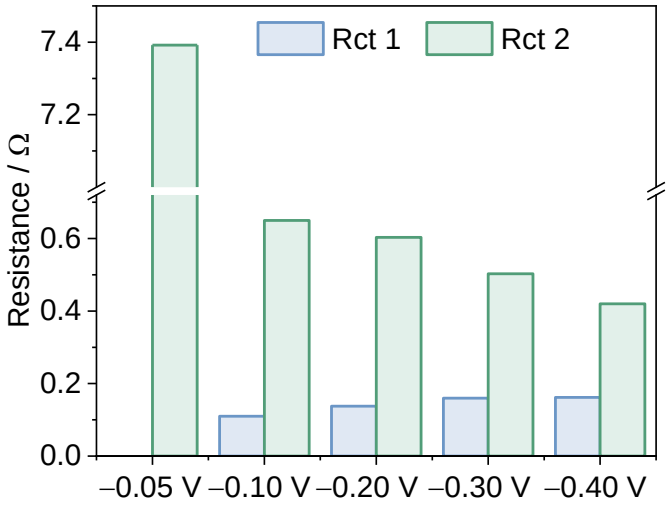

Supplementary Fig. 31| Rct 1 and Rct 2 of Pt-oxo NPs at different applied potentials based on Fig. 4e.

Supplementary Table 4. Potential-dependent Nyquist plots of Pt-oxo NPs at different applied potentials.

η	Rs	T-1	P-1	Rct-1	T-2	P-2	Rct-2	C_{dl}
–0.05 V	0.63964	0	0	0	0.019	0.82804	7.3917	0.000424118
–0.10 V	1.3922	0.0022974	0.92616	0.11	0.12433	0.76029	0.65	0.000639635
–0.20 V	1.0157	0.0046591	0.85102	0.13758	0.1077	0.77417	0.60314	0.000752603
–0.30 V	1.3038	0.0071601	0.75308	0.15985	0.11593	0.80418	0.50268	0.001853903
–0.40 V	1.3902	0.019783	0.71649	0.1619	0.15	0.84	0.42	0.006063161

Supplementary Note 6. The effective double-layer capacitance (C_{dl}) was obtained from the constant phase element (CPE2) parameters and the two resistances via the Brug formula:

$$C_{\mathrm{dl}} = T^{\frac{1}{P}}\left(\frac{1}{Rs} + \frac{1}{Rct}\right)^{\frac{P-1}{P}}$$

where *R*s is the solution resistance, *R*ct2 is the charge transfer resistance, *T* is the CPE2 constant, and *P* is the CPE2 exponent.

The EIS fitting parameters were obtained via the following equivalent circuit:

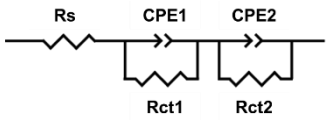

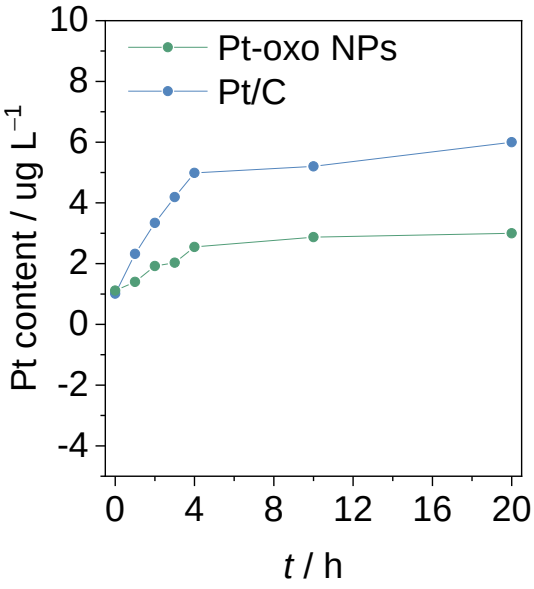

Supplementary Fig. 32| Contents of Pt in the electrolytes during HER operation at –200 mA cm^{-2} for 20 h with Pt-oxo NPs and Pt/C as the electrocatalyst.

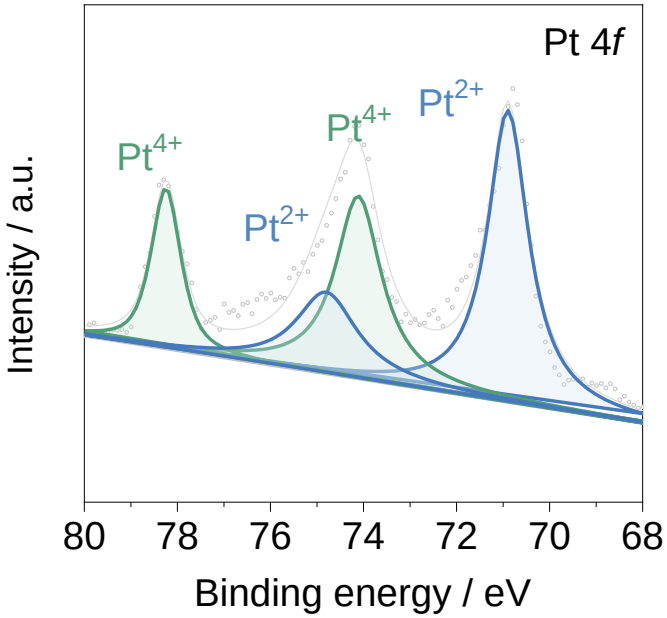

Supplementary Fig. 33| Pt 4f XPS spectra of the Pt-oxo NPs after shutdown for 20 h.

Supplementary Note 7. As shown in Supplementary Fig. 33, the Pt valence state of the Pt-oxo NPs essentially remained unchanged after 20 h of shutdown compared with the initial state (Fig. 2b).

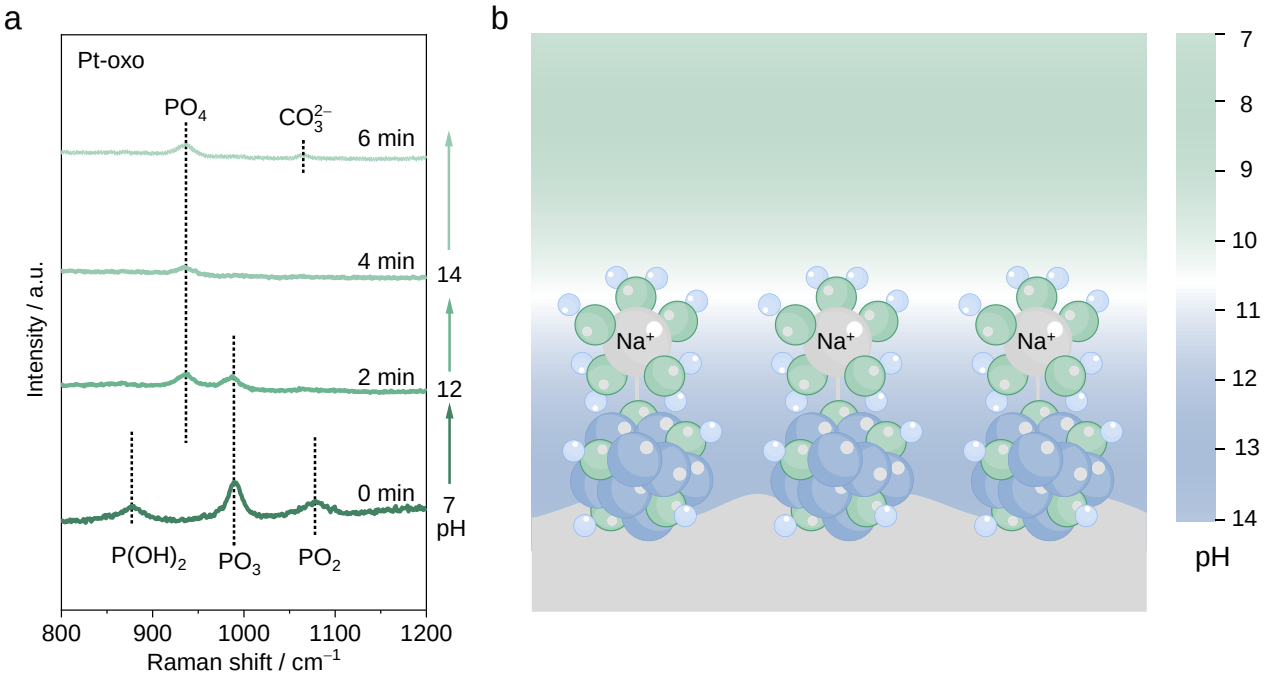

Supplementary Fig. 34| Phosphate species used as Raman probes to monitor local pH changes during the shutdown period. a, Time-dependent Raman spectra of the Pt-oxo NPs recorded at the electrode interface during the shutdown period with phosphate species as pH probes. **b**, Interfacial pH variations on the Pt-oxo NPs during the shutdown period.

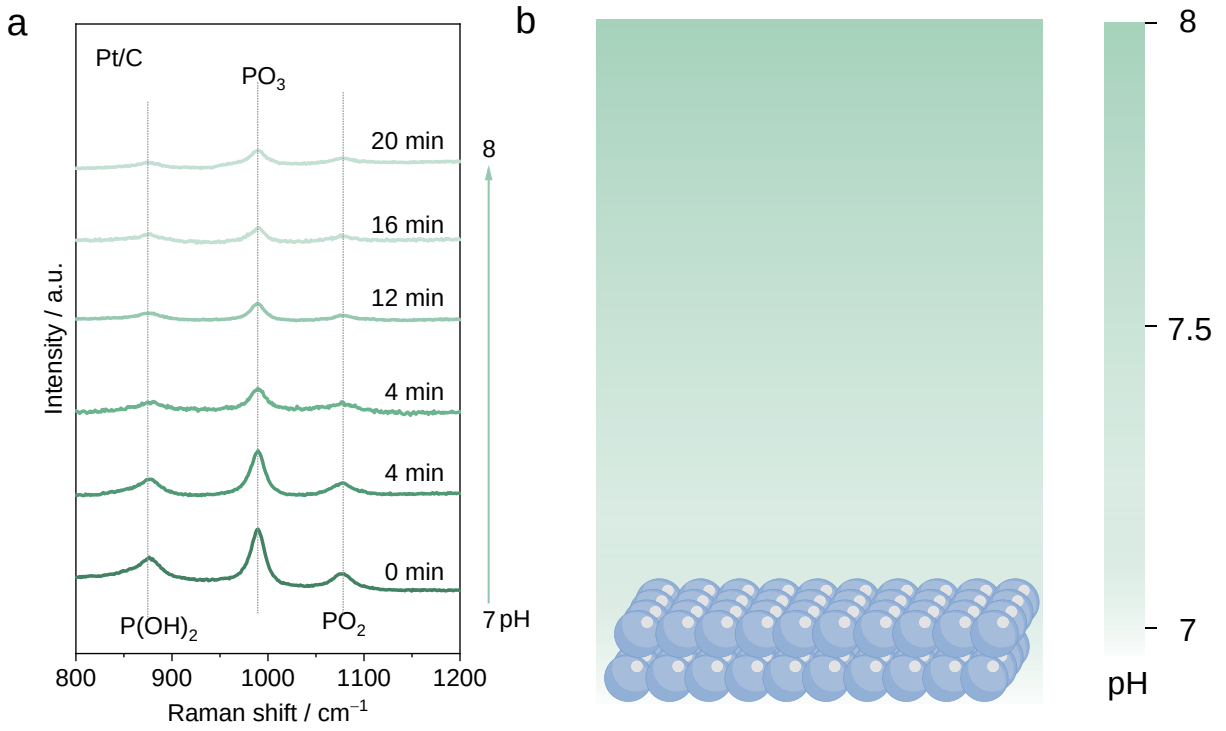

Supplementary Fig. 35| Phosphate species used as Raman probes to monitor local pH changes during the shutdown period. a, Time-dependent Raman spectra of Pt/C recorded at the electrode interface during the shutdown period with phosphate species as pH probes. **b**, Interfacial pH variations on Pt/C during the shutdown period.

Supplementary Note 8. Measurement of the local pH at the electrode surface during the shutdown period. The distribution of OH^- ions at the electrode interface of the Pt-oxo NPs and Pt/C during the shutdown period was evaluated by monitoring the interfacial pH variations. PBS (pH=7) (1.0 M) was employed as the electrolyte, in which phosphate species acted as pH-sensitive probes to enable in situ Raman spectroscopy monitoring of interfacial pH variations. According to the relationship between pH and phosphate species reported previously[34], the initial electrolyte has three peaks, PO_2 (1076 cm^{-1}), PO_3 (990 cm^{-1}), and $P(OH)_2$ (877 cm^{-1}), suggesting a pH of 7. After shutdown for 2 min, the peaks of PO_2 and $P(OH)_2$ disappeared from the surface of the Pt-oxo NPs, and a new peak corresponding to PO_4 appeared at 936 cm^{-1}, suggesting that the pH increased to 12 (Supplementary Fig. 34a). After being shut down for 4 min, PO_3 also disappears, indicating that the pH has reached 14. Accordingly, the OH^- concentration clearly exhibited a spatial gradient from the surface to the bulk (Supplementary Fig. 34b), confirming the aggregation of OH^- through the

Pt-O-Na^+ structure. Conversely, there was no change in the pH of the surface of Pt/C within 20 min (Supplementary Fig. 35). Collectively, these results reveal that the aggregated Na^+ promotes the activation of water to produce a large amount of OH^- with the depletion of protons, whereas the diffusion of OH^- to the bulk electrolyte is severely inhibited by the Na^+ on the surface of the Pt-oxo NPs, leading to the enrichment of OH^- outside the Pt-O-Na^+ structure.

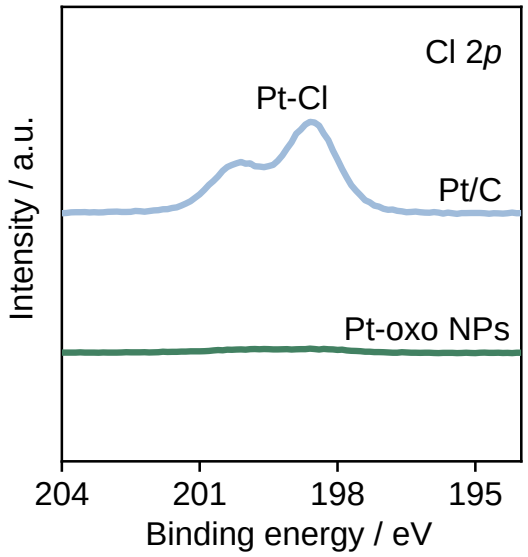

Supplementary Fig. 36| Cl 2*p* XPS spectra of the Pt-oxo NPs, Pt NPs, and Pt/C after shutdown for 20 h.

Supplementary Note 9. As shown in Supplementary Fig. 36, the formation of Pt–Cl bonds[35] on the surface of Pt/C after a 20 h shutdown indicates that Pt/C is poisoned by Cl^- in seawater, whereas the accumulation of abundant OH^- via the Pt-O-Na^+ of Pt-oxo NPs hinders the poisoning of Cl^-.

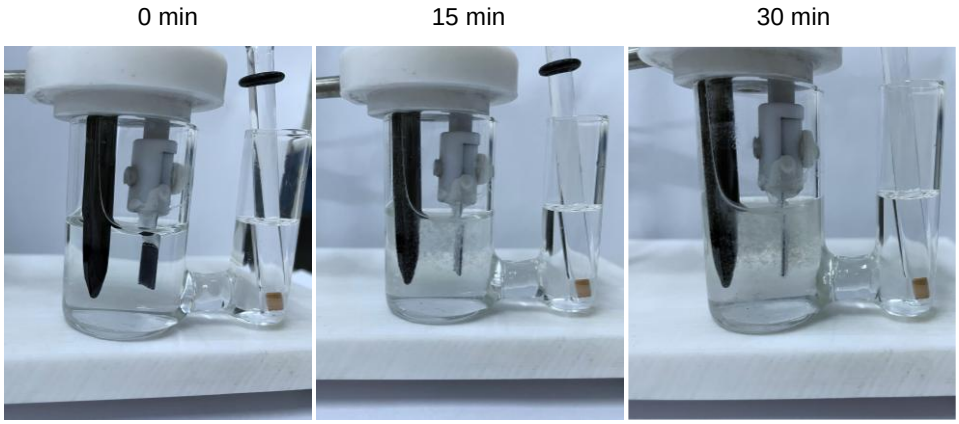

Supplementary Fig. 37| Observation of precipitation formation within 30 min on Pt/C cathodes at –200 mA cm^{-2}.

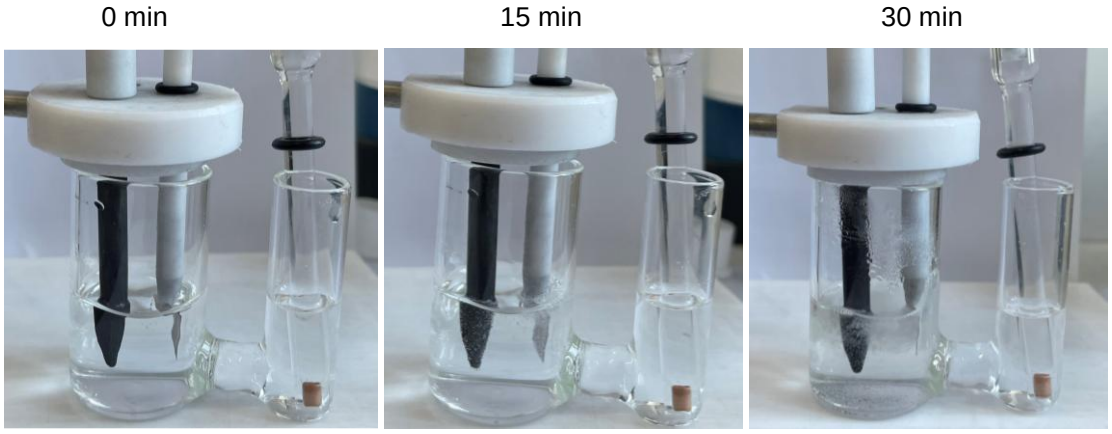

Supplementary Fig. 38| Observation of precipitation formation within 30 min on Pt NPs cathodes at –200 mA cm^{-2}.

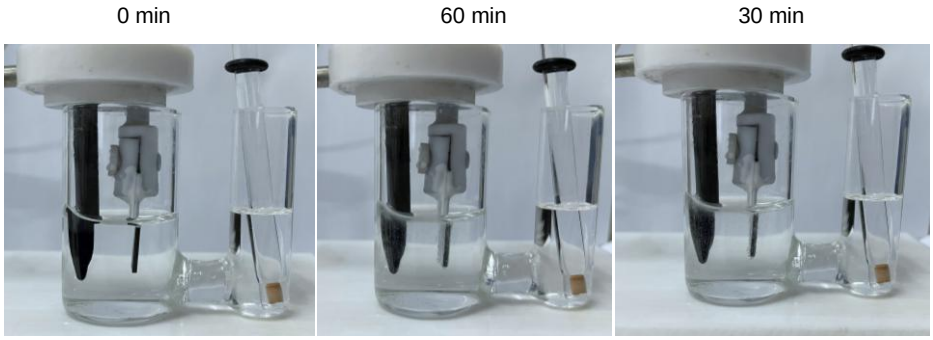

Supplementary Fig. 39| Observation of precipitation formation within 60 min on Pt-oxo NPs cathodes at –200 mA cm^{-2}.

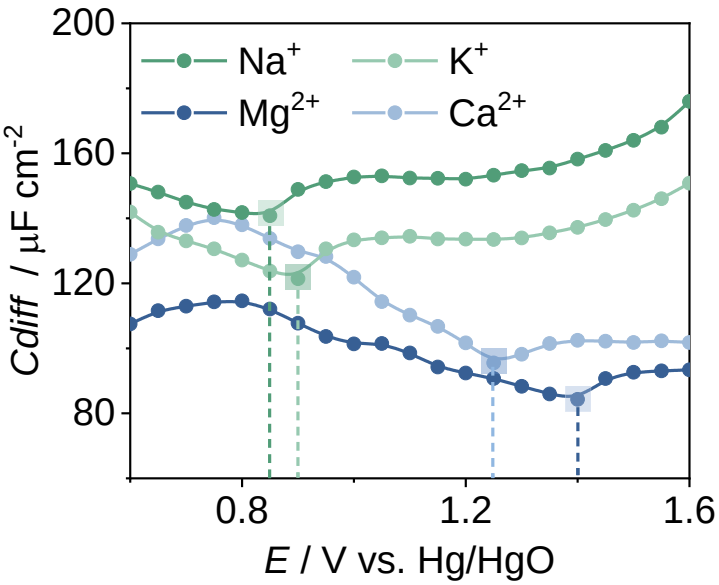

Supplementary Fig. 40| Zero charge (PZC) of Pt-oxo NPs in equimolar charge quantities of $CaSO_4$, $MgSO_4$, Na_2SO_4, and K_2SO_4.

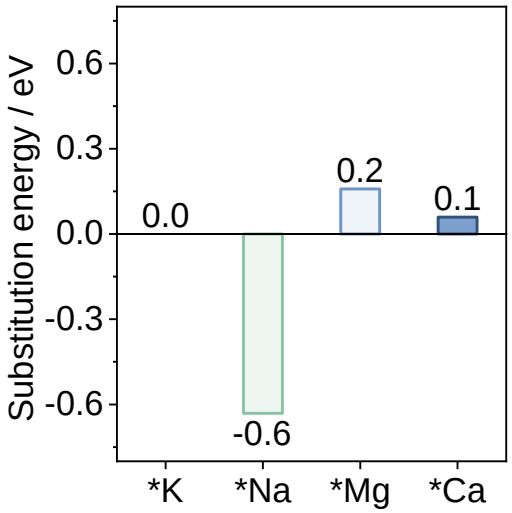

Supplementary Fig. 41| Substitution energy of cations on the surface of Pt-oxo NPs.

Supplementary Note 10. Through AIMD and DFT calculations, the state of the Pt-oxo in the electrolyte was simulated. We selected a K ion adsorbed on the surface of the Pt-oxo as a reference and replaced the K ions with Na, Mg, and Ca ions. The substitution energy ($\Delta E = E_{\text{Pt-oxo+Na/Mg/Ca}} + E_{\text{K}} - E_{\text{Pt-oxo+K}} - E_{\text{Na/Mg/K}}$) of the ions at this site was calculated to evaluate the stability of the ions on the Pt-oxo surface.

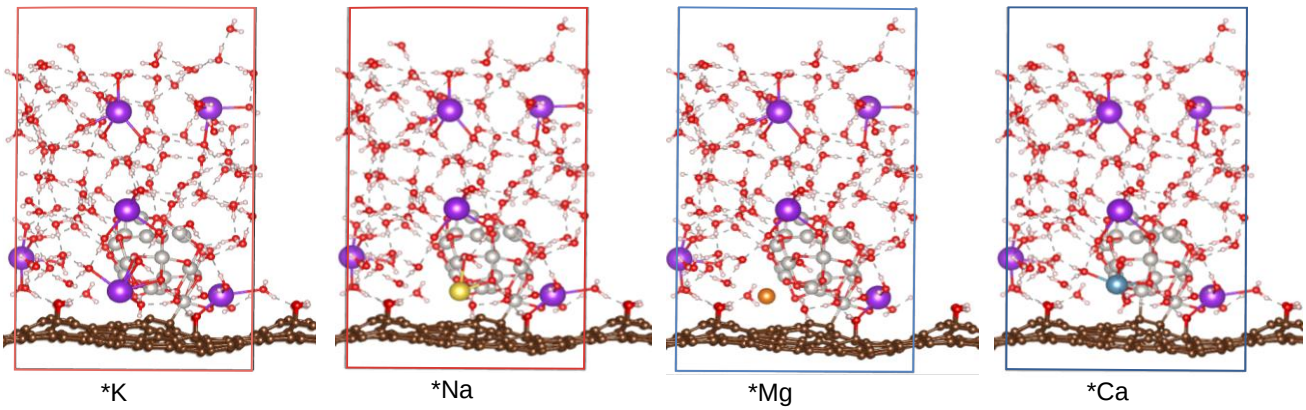

Supplementary Fig. 42| Cation models on the surface of Pt-oxo NPs according to Supplementary Fig. 41.

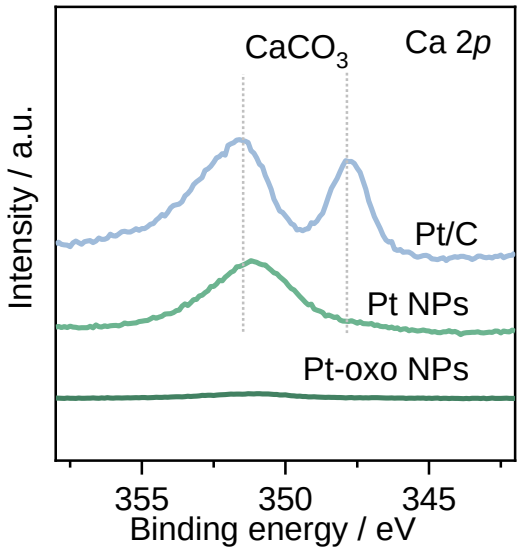

Supplementary Fig. 43| Ca 2p XPS spectra of the Pt-oxo NPs, Pt NPs, and Pt/C after the HER operation period.

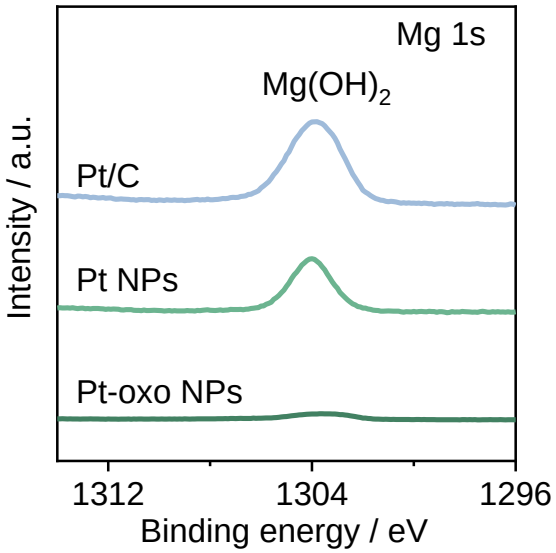

Supplementary Fig. 44| Mg 1*s* XPS spectra of the Pt-oxo NPs, Pt NPs, and Pt/C after the HER operation period.

Supplementary Note 11. After activation, $CaCO_3$ and $Mg(OH)_2$ species are formed on the surfaces of both the Pt/C and Pt NPs (Supplementary Figs. 43–44). In contrast, the surface of the Pt-oxo NPs shows no signals of Ca/Mg-related precipitates, which is in agreement with the other characteristic results.

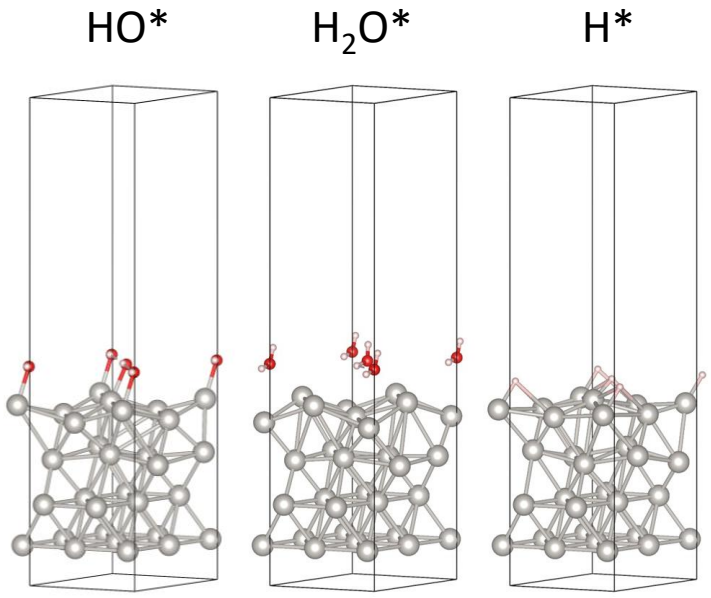

Supplementary Fig. 45| Theoretical models of HO*, H_2O*, and H* adsorbed on Pt.

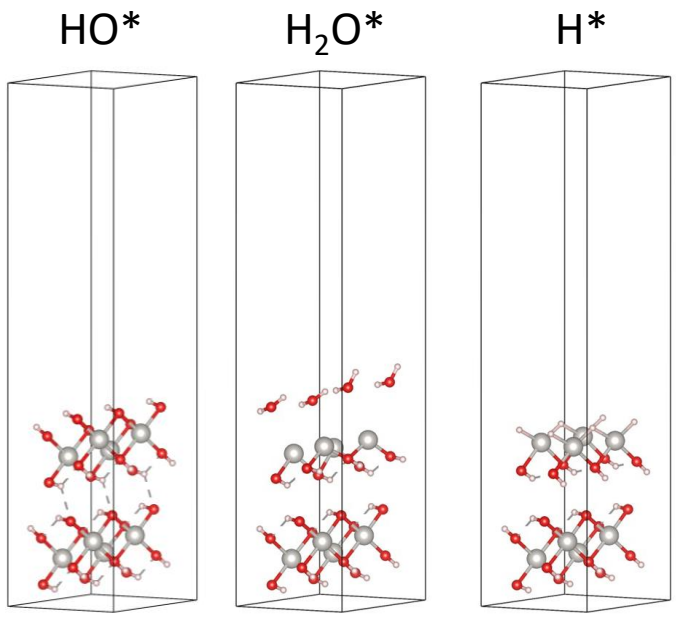

Supplementary Fig. 46| Theoretical models of HO*, H_2O*, and H* adsorbed on $Pt(OH)_2$.

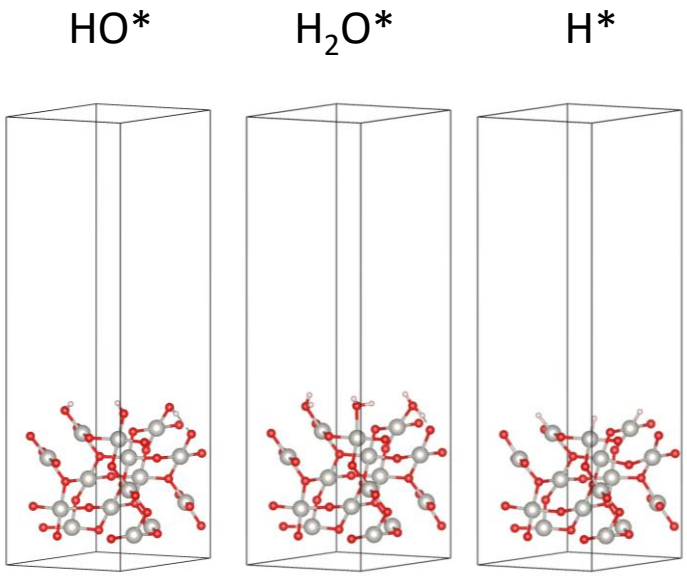

Supplementary Fig. 47| Theoretical models of HO*, H_2O*, and H* adsorbed on Pt_3O_4.

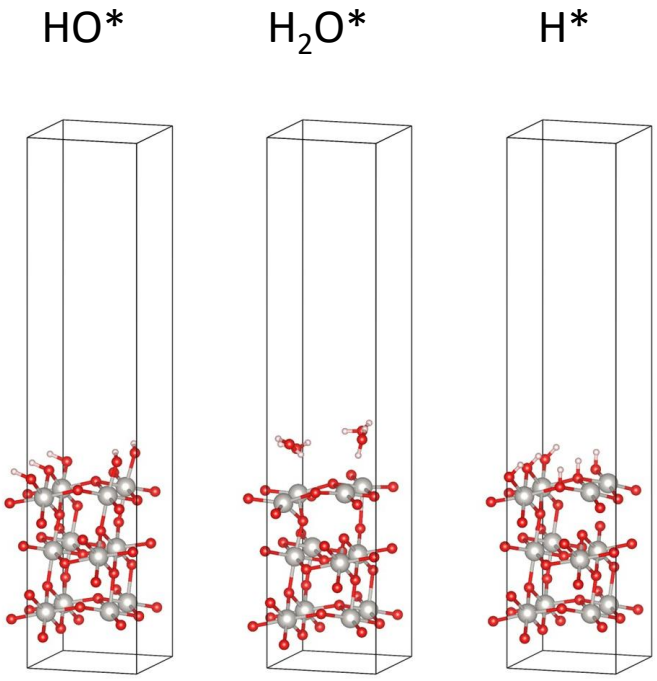

Supplementary Fig. 48| Theoretical models of HO*, H_2O*, and H* adsorbed on PtO_2.

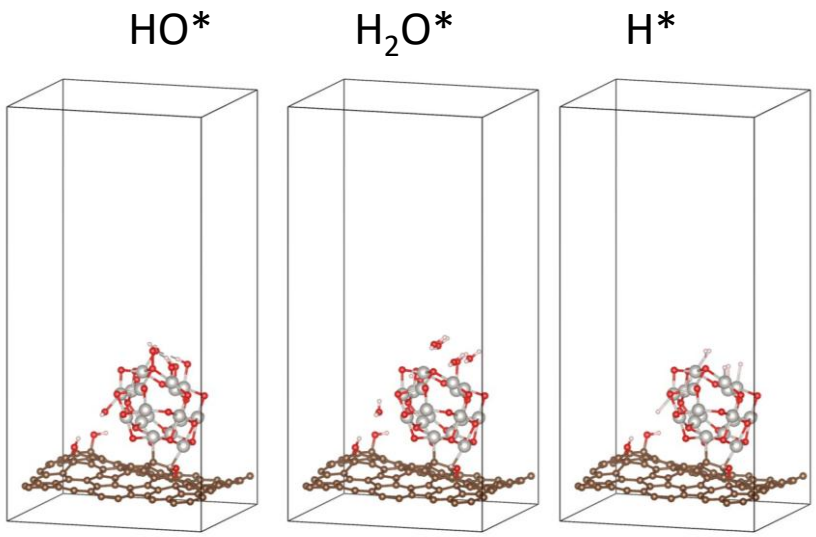

Supplementary Fig. 49| Theoretical models of HO*, H_2O*, and H* adsorbed on PtO_x.

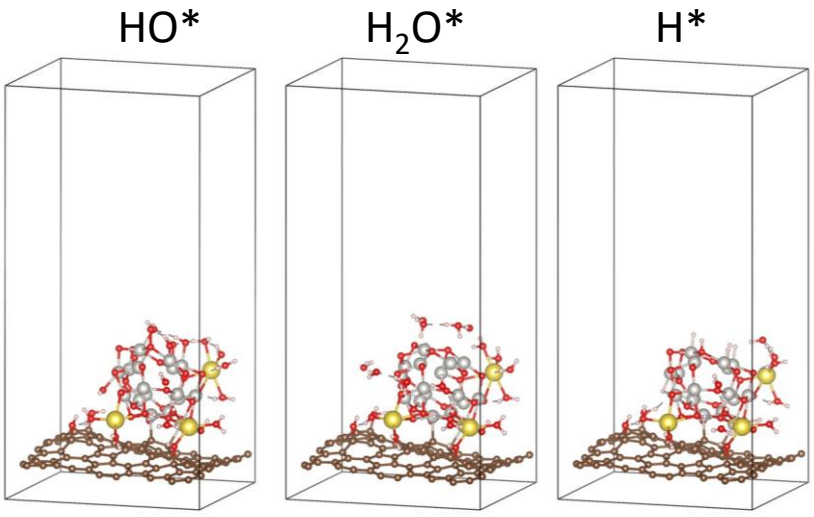

Supplementary Fig. 49| Theoretical models of HO*, H_2O*, and H* adsorbed on Pt-O-Na^+.

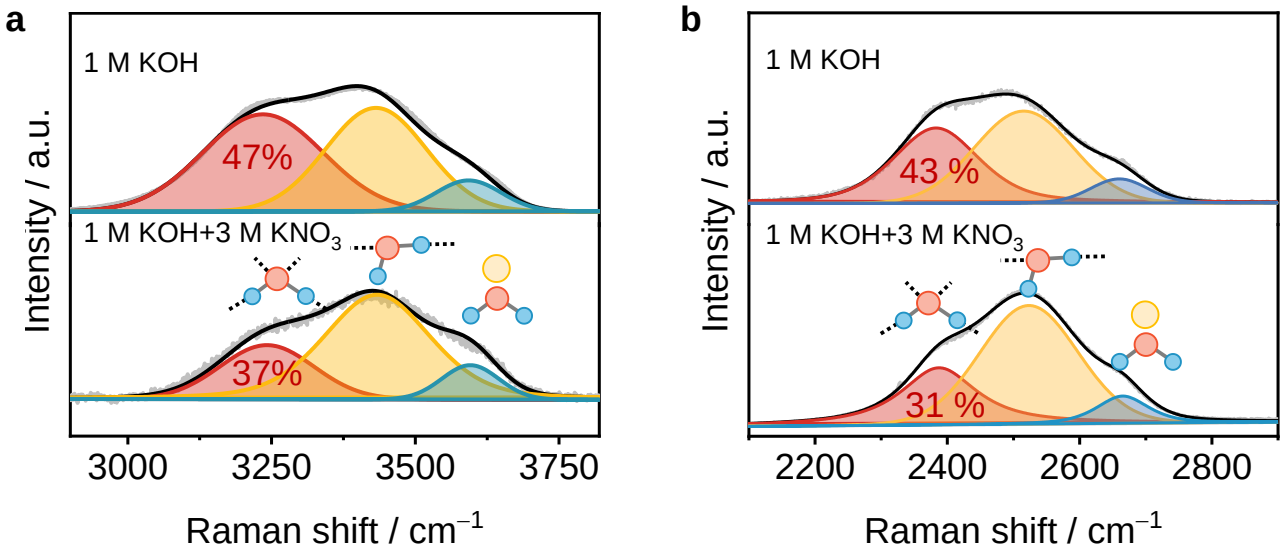

Supplementary Fig. 51| Monitoring of HB during the synthesis of Pt-oxo NPs in different electrolytes via Raman spectroscopy. HB near the Pt-oxo nanoparticle surface in 1.0 M KOH and 1.0 M KOH + 3.0 M KNO_3, as revealed by Raman spectroscopy with (**a**) H_2O and (**b**) D_2O as the solvents.

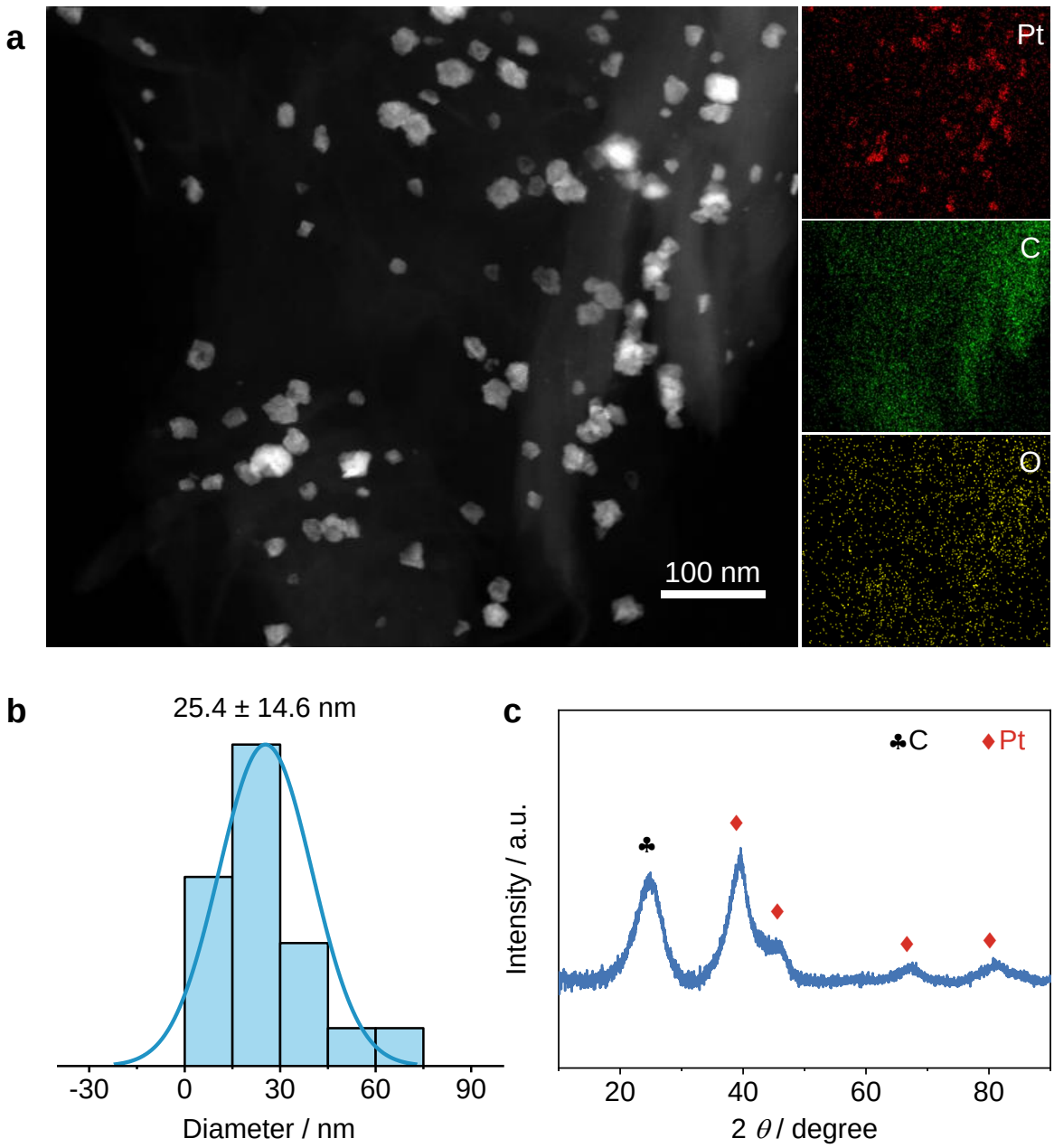

Supplementary Fig. 52| Synthesis of Pt-oxo NPs in 1.0 M KOH + 3.0 M KNO_3. a, HAADF−HRTEM image and elemental mapping images. **b**, Particle size distribution histogram. **c**, XRD pattern.

Supplementary Note 12. HBs play crucial roles in stabilizing the valence state and particle size of Pt-oxo NPs. The HB network in solution is supposed to greatly contribute to stabilizing ultrasmall Pt-oxo NPs. To verify this assumption, we adopted an electrolyte with a high K^+ ion content (1.0 M KOH + 3.0 M KNO_3) to disrupt the HBs network near the electrode surface. In the Raman spectra,

the peaks at 3235, 3431, and 3592 cm^{-1} represent water with 4 HB, 2 HB, and K^+–H_2O, respectively[42]. The high concentration of K^+ ions decreases the population of the 4 HB from 47% (1.0 M KOH) to 37% (red peaks in Supplementary Fig. 45a). Isotope-labelled Raman spectra further confirmed the above conclusions (Supplementary Fig. 45b). Accordingly, the size of the prepared Pt-oxo NPs increased rapidly from 1.0 nm to 25.4 nm (Supplementary Fig. 46a–b), accompanied by the formation of crystalline Pt (Supplementary Fig. 46c), indicating the important ability of the HBs network as a shield to protect the size and valence of the Pt-oxo NPs.

Supplementary References

1 Kresse, G. & Furthmüller, J. Efficient iterative schemes for ab initio total-energy calculations using a plane-wave basis set. *Phys. Rev. B* **54**, 11169(1996).

2 Blöchl, P. E. Projector augmented-wave method. *Phys. Rev. B* **50**, 17953(1994).

3 Perdew, J. P., Burke, K. & Ernzerhof, M. Generalized gradient approximation made simple. *Phys. Rev. Lett.* **77**, 3865(1996).

4 Mathew, K., Sundararaman, R., Letchworth-Weaver, K., Arias, T. A. & Hennig, R. G. Implicit solvation model for density-functional study of nanocrystal surfaces and reaction pathways. *J. Chem. Phys.* **140**, 084106(2014).

5 Lu, S., Shi, Y., Zhou, W., Zhang, Z., Wu, F. & Zhang, B. Dissolution of the heteroatom dopants and formation of ortho-quinone moieties in the doped carbon materials during water electrooxidation. *J. Am. Chem. Soc.* **144**, 3250–3258(2022).

6 Tsounis, C., Subhash, B., Kumar, P. V., Bedford, N. M., Zhao, Y., Shenoy, J., Ma, Z., Zhang, D., Toe, C. Y. & Cheong, S. Pt single atom electrocatalysts at graphene edges for efficient alkaline hydrogen evolution. *Advanced Functional Materials* **32**, 2203067(2022).

7 Abbas, S. A., Iqbal, M. I., Kim, S. H. & Jung, K. D. Catalytic Activity of Urchin-like Ni nanoparticles Prepared by Solvothermal Method for Hydrogen Evolution Reaction in Alkaline Solution. *Electrochimica Acta* **227**, 382-390(2017).

8 Xiaoxin, Zou, Xiaoxi, Huang, Anandarup, Goswami, Rafael, Silva, Bhaskar & R. Cobalt-Embedded Nitrogen-Rich Carbon Nanotubes Efficiently Catalyze Hydrogen Evolution Reaction at All pH Values. *Angewandte Chemie International Edition*(2013).

9 Sheng, W., Gasteiger, H. A. & Shao-Horn, Y. Hydrogen Oxidation and Evolution Reaction Kinetics on Platinum: Acid vs Alkaline Electrolytes. *Journal of The Electrochemical Society* **157**, B1529(2010).

10 Xue, Z.-H., Su, H., Yu, Q.-Y., Zhang, B., Wang, H.-H., Li, X.-H. & Chen, J.-S. Janus Co/CoP Nanoparticles as Efficient Mott–Schottky Electrocatalysts for Overall Water Splitting in Wide pH Range. *Advanced Energy Materials* **7**, 1602355(2017).

11 Huang, S., Meng, Y., He, S., Goswami, A., Wu, Q., Li, J., Tong, S., Asefa, T. & Wu, M. N-, O-, and S-Tridoped Carbon-Encapsulated Co9S8 Nanomaterials: Efficient Bifunctional Electrocatalysts for Overall Water Splitting. *Advanced Functional Materials* **27**, 1606585(2017).

12 Xu, W., Zhao, R., Li, Q., Sun, B., Wu, J., Zhong, W., Gao, Y., Nan, X., Huang, Q. & Yang, Y. Overall water splitting on the NiS/NiS2 heterostructures featuring self-equilibrium orbital occupancy. *Advanced Energy Materials* **13**, 2300978(2023).

13 Wang, X., Zhang, Y., Li, J., Liu, G., Gao, M., Ren, S., Liu, B., Zhang, L., Han, G. & Yu, J. Platinum cluster/carbon quantum dots derived graphene heterostructured carbon nanofibers for efficient and durable solar-driven electrochemical hydrogen evolution. *Small Methods* **6**, 2101470(2022).

14 Luo, X., Yuan, P., Xiao, H., Li, S., Luo, J., Li, J., Lai, W., Chen, Y. & Li, D. Effects of intrinsic defects in Pt-based carbon supports on alkaline hydrogen evolution reaction. *ACS Applied Materials & Interfaces* **16**, 26044-26056(2024).

15 Pi, M., Wu, T., Guo, W., Wang, X., Zhang, D., Wang, S. & Chen, S. Phase-controlled synthesis of polymorphic tungsten diphosphide with hybridization of monoclinic and orthorhombic phases as a novel electrocatalyst for efficient hydrogen evolution. *Journal of Power Sources* **349**,

138-143(2017).
16 Wang, S., Yuan, D., Sun, S., Huang, S., Wu, Y., Zhang, L., Dou, S. X., Liu, H. K., Dou, Y. & Xu, J. Iron, Tungsten Dual-Doped Nickel Sulfide as Efficient Bifunctional Catalyst for Overall Water Splitting. *Small* **20**, 2311770(2024).
17 Zeng, L., Zhao, Z., Huang, Q., Zhou, C., Chen, W., Wang, K., Li, M., Lin, F., Luo, H., Gu, Y., Li, L., Zhang, S., Lv, F., Lu, G., Luo, M. & Guo, S. Single-atom Cr-N_4 sites with high oxophilicity interfaced with Pt atomic clusters for practical alkaline hydrogen evolution catalysis. *J. Am. Chem. Soc.* **145**, 21432–21441(2023).
18 Poudel, M. B., Logeshwaran, N., Prabhakaran, S., Kim, A. R., Kim, D. H. & Yoo, D. J. Low-cost hydrogen production from alkaline/seawater over a single-step synthesis of Mo_3Se_4-NiSe core–shell nanowire arrays. *Advanced Materials* **36**, 2305813(2024).
19 Wang, L., Hao, Y., Deng, L., Hu, F., Zhao, S., Li, L. & Peng, S. Rapid complete reconfiguration induced actual active species for industrial hydrogen evolution reaction. *Nature Communications* **13**, 5785(2022).
20 Guo, J., Zheng, Y., Hu, Z., Zheng, C., Mao, J., Du, K., Jaroniec, M., Qiao, S.-Z. & Ling, T. Direct seawater electrolysis by adjusting the local reaction environment of a catalyst. *Nature Energy* **8**, 264-272(2023).
21 Xiu, L., Pei, W., Zhou, S., Wang, Z., Yang, P., Zhao, J. & Qiu, J. Multilevel hollow MXene tailored Low-Pt catalyst for efficient hydrogen evolution in full-pH range and seawater. *Advanced Functional Materials* **30**, 1910028(2020).
22 Liang, J., Cai, Z., Li, Z., Yao, Y., Luo, Y., Sun, S., Zheng, D., Liu, Q., Sun, X. & Tang, B. Efficient bubble/precipitate traffic enables stable seawater reduction electrocatalysis at industrial-level current densities. *Nat. Commun.* **15**, 2950(2024).
23 Wu, X., Zhou, S., Wang, Z., Liu, J., Pei, W., Yang, P., Zhao, J. & Qiu, J. Engineering multifunctional collaborative catalytic interface enabling efficient hydrogen evolution in all pH range and seawater. *Advanced Energy Materials* **9**, 1901333(2019).
24 Zhu, J., Chi, J., Cui, T., Guo, L., Wu, S., Li, B., Lai, J. & Wang, L. F doping and P vacancy engineered FeCoP nanosheets for efficient and stable seawater electrolysis at large current density. *Applied Catalysis B: Environmental* **328**, 122487(2023).
25 Xu, W., Ma, T., Chen, H., Pan, D., Wang, Z., Zhang, S., Zhang, P., Bao, S., Yang, Q. & Zhou, L. Scalable fabrication of Cu_2S@NiS@Ni/NiMo hybrid cathode for high–performance seawater electrolysis. *Advanced Functional Materials* **33**, 2302263(2023).
26 Liu, L., Lu, J., Yang, Y., Ruettinger, W., Gao, X., Wang, M., Lou, H., Wang, Z., Liu, Y. & Tao, X. Dealuminated Beta zeolite reverses Ostwald ripening for durable copper nanoparticle catalysts. *Science* **383**, 94–101(2024).
27 Gu, X., Yu, M., Chen, S., Mu, X., Xu, Z., Shao, W., Zhu, J., Chen, C., Liu, S. & Mu, S. Coordination environment of Ru clusters with in-situ generated metastable symmetry-breaking centers for seawater electrolysis. *Nano Energy* **102**, 107656(2022).
28 Ning, M., Wang, Y., Wu, L., Yang, L., Chen, Z., Song, S., Yao, Y., Bao, J., Chen, S. & Ren, Z. Hierarchical interconnected NiMoN with large specific surface area and high mechanical strength for efficient and stable alkaline water/seawater hydrogen evolution. *Nano-Micro Letters* **15**, 157(2023).
29 Li, S., Zhuo, Y., Liu, D., Pan, H. & Wang, Z. Anchoring highly surface-exposed Pt single atoms on Ni_3S_2/Co_9S_8 with abundant S vacancies triggers d-orbital electron rearrangements for boosted

seawater hydrogen evolution. *Applied Catalysis B: Environment and Energy* **355**, 124188(2024).
30 Li, M., Li, H., Fan, H., Liu, Q., Yan, Z., Wang, A., Yang, B. & Wang, E. Engineering interfacial sulfur migration in transition-metal sulfide enables low overpotential for durable hydrogen evolution in seawater. *Nature Communications* **15**, 6154(2024).
31 Xie, H., Zhao, Z., Liu, T., Wu, Y., Lan, C., Jiang, W., Zhu, L., Wang, Y., Yang, D. & Shao, Z. A membrane-based seawater electrolyser for hydrogen generation. *Nature* **612**, 673-678(2022).
32 Kang, X., Yang, F., Zhang, Z., Liu, H., Ge, S., Hu, S., Li, S., Luo, Y., Yu, Q. & Liu, Z. A corrosion-resistant RuMoNi catalyst for efficient and long-lasting seawater oxidation and anion exchange membrane electrolyzer. *Nat. Commun.* **14**, 3607(2023).
33 Fan, R., Liu, C., Li, Z., Huang, H., Feng, J., Li, Z. & Zou, Z. Ultrastable electrocatalytic seawater splitting at ampere-level current density. *Nature Sustainability* **7**, 158-167(2024).
34 Lu, S., Zhang, Z., Zhang, B. & Shi, Y. Insight into the change in local pH near the electrode surface using phosphate species as the probe. *J. Phys. Chem. Lett.* **14**, 10457–10462(2023).
35 Chastain, J. & King Jr, R. C. Handbook of X-ray photoelectron spectroscopy. *Perkin-Elmer Corporation* **40**, 25(1992).